Fast event-based electron counting for small molecule structure determination by MicroED

Niko Vlahakis[1], Songrong Qu[1], Logan S. Richards[1], Lygia Silva de Moraes[2], Duilio Cascio[1], Hosea M. Nelson[2] and Jose A. Rodriguez[1]

[1] Department of Chemistry and Biochemistry; UCLA-DOE Institute for Genomics and Proteomics; STROBE, NSF Science and Technology Center; University of California, Los Angeles (UCLA); Los Angeles, CA 90095, USA.

[2] Division of Chemistry and Chemical Engineering, California Institute of Technology, Pasadena, California, 91125, USA

Correspondence: Jose A. Rodriguez (jrodriguez@mbi.ucla.edu)

Synopsis Fast readout event-based electron counting (EBEC) is a promising detection strategy to determine accurate *ab initio* structures of beam-sensitive small molecules by MicroED. A fast EBEC approach enhances the dynamic range of MicroED data by limiting the likelihood of coincidence loss (CL) - the undercounting of electrons due to their temporally or spatially unresolved arrival on a direct electron detector. As implemented by new counting detectors, fast EBEC allows structure-worthy datasets to be captured from individual small molecule crystals in under a minute.

Abstract Electron counting helped realize the resolution revolution in single particle cryoEM and is now accelerating the determination of MicroED/3DED structures. Its advantages are best demonstrated by new direct electron detectors capable of fast (kilohertz) event-based electron counting (EBEC). This strategy minimizes the inaccuracies introduced by coincidence loss (CL) and promises fast, accurate structures. We use the Direct Electron Apollo camera to leverage EBEC technology for MicroED data collection. Given its ability to count single electrons, the Apollo collects high quality MicroED data from organic small molecule crystals illuminated with incident electron beam flux values as low as 0.01–0.045 $e^-/Å^2/s$. Under even the lowest flux (0.01 $e^-/Å^2/s$) condition, fast EBEC data produced *ab initio* structures of a salen ligand (268 Da) and biotin (244 Da). Each structure was determined from 100–degree wedge of data collected from a single crystal in as few as 50 seconds, with a delivered fluence of only ~0.5 $e^-/Å^2$. Fast EBEC data collected with a fluence of 2.25 or 3.33 $e^-/Å^2$ also facilitated a 1.5Å structure of thiostrepton (1,665 Da). While refinement of those structures appeared unaffected by CL, a CL-adjustment applied to gain-normalized EBEC data further improved the distribution of intensities measured from salen ligand and biotin crystals. However, CL-adjustment only marginally improved the refinement of their corresponding structures, signaling the already high counting accuracy of detectors with counting rates in the kilohertz range. Overall, by delivering low-dose structure-worthy data, fast EBEC collection strategies open new possibilities for high-throughput MicroED.

1. Introduction

Microcrystal electron diffraction (MicroED), also referred to as three-dimensional electron diffraction (3DED) is sought out for its ability to interrogate a variety of micro-scale or nano-scale crystallites (Saha *et al.*, 2022), including proteins (Shi *et al.*, 2013), peptides (Rodriguez *et al.*, 2015), small molecules (Jones *et al.*, 2018) and materials (Wang *et al.*, 2018). One key to the success of MicroED has been its adoption of existing crystallographic approaches and cryoEM instrumentation for the determination of atomic structures (Rodriguez *et al.*, 2017). Over the past decade, the typical MicroED experiment has relied on the use of a transmission electron microscope (TEM) equipped with an electron source operating at 200–300keV and fitted with a scintillator-based pixelated detector. In this way, TEMs have been, without much alteration, readily adaptable to MicroED experiments at room temperature or under cryogenic conditions (Saha *et al.*, 2022). MicroED has also benefitted from the robustness of crystallographic theory and its application, broadly adopting the implementation of crystallographic data reduction and refinement software (Kabsch, 2010; Winter *et al.*, 2018; Dolomanov *et al.*, 2009; Adams *et al.*, 2010; Murshudov *et al.*, 2011; Emsley & Cowtan, 2004; Sheldrick, 2015, 2008).

Several recent advances have expanded the applicability of MicroED. These include updated sample preparation methodologies, such as focused ion beam milling (Duyvesteyn *et al.*, 2018; Martynowycz *et al.*, 2019; Parkhurst *et al.*, 2023), pressure-assisted sample deposition and use of microarray robotics (Zhao *et al.*, 2021; Delgadillo *et al.*, 2024). Likewise, software developments have improved the likelihood of determining challenging beam-sensitive samples and, in some cases, informing on their chiral nature (Saha *et al.*, 2022; Palatinus *et al.*, 2017; Brázda *et al.*, 2019), complementing electron nanobeam and serial diffraction approaches that improve greater throughput, and extract crystallographic information from minuscule collections of molecules (Bücker *et al.*, 2020; Gallagher-Jones *et al.*, 2020; Hogan-Lamarre *et al.*, 2024). Some of these new developments have specifically leveraged new commercial or experimental (Saha *et al.*, 2023) direct electron detectors (DED), illuminating the promise of these types of sensors for diffraction.

The growing adoption of DEDs for diffraction data collection echoes their successful application to single particle cryoEM (Wu *et al.*, 2016). However, diffraction experiments represent a unique challenge for DEDs, particularly when performing electron counting, because of coincidence loss (CL) (Li *et al.*, 2013; McMullan *et al.*, 2014; Gallagher-Jones *et al.*, 2019; Hattne *et al.*, 2023). When imaging in real space, a DED can anticipate a nearly flat illumination across its surface. In this mode, it must count individual events landing at a given rate, with relatively equal likelihood, on any one of its pixels (Li *et al.*, 2013). This allows interpretable images to be recorded at low flux, with a limited dynamic range detector. By contrast, diffraction from highly ordered crystals requires accurate counting across a wide dynamic range. A large number of electrons must be accurately counted at high-intensity reflections, while single electrons must be registered at the weakest reflections.

Since the distribution of crystal reflection intensities on a detector is difficult to anticipate *a priori*, any pixel on the sensor must be able to deliver the full dynamic range at any given time. This presents a challenge for most commercially available DEDs, which have low readout and internal counting or frame rates that fundamentally limit the number of electrons measurable per pixel per second. Exceeding these limits results in CL, which effectively narrows the dynamic range of observable signal. Despite these challenges, several studies have demonstrated the utility of electron counting for electron diffraction data collection. For example, in 2019, a K2 detector was used to chart the nanoscale mosaicity of peptide crystals using nanobeam diffraction (Gallagher-Jones *et al.*, 2019); challenges with CL were notable under those conditions. Follow-up work in 2020 led to the structure of a hexapeptide nanocrystal determined *ab initio* from electron nanobeam diffraction data, also collected on a K2 detector in counting mode (Gallagher-Jones *et al.*, 2020). More recently, similar detectors have been used to determine *ab initio* structures of macromolecules (Martynowycz *et al.*, 2022), with specific data collection settings implemented to minimize CL while retaining high-resolution signal (Hattne *et al.*, 2023; Clabbers, Martynowycz, Hattne, Nannenga *et al.*, 2022).

Most MicroED experiments using DEDs in counting mode have required severe restriction of incident electron beam flux on the crystal. This lowering of beam flux is often compensated for by extending integration and overall data collection times (Martynowycz *et al.*, 2022; Clabbers, Martynowycz, Hattne, & Gonen, 2022; Clabbers, Martynowycz, Hattne, Nannenga *et al.*, 2022; Takaba *et al.*, 2021). The need for drastic flux reduction depends on the type of DED used, and its internal count rate. For example, new hybrid pixel detector (HPD) technologies have overcome these limitations to enable fast serial electron diffraction (SerialED) data collection (Bücker *et al.*, 2020). However, the advantage afforded by the speed and sensitivity of HPDs is at odds with their larger pixel size and limited sensor pixel density compared to monolithic active pixel sensors (Peng *et al.*, 2023). In detectors such as the Apollo (Direct Electron), on-chip event-based thresholding and registration addresses the need for high-speed counting while reducing the burden of handling and processing large amounts of raw data (Peng *et al.*, 2023). This implementation permits kilohertz-rate event-based electron counting (EBEC). The use of field programable gate arrays (FPGA) for downstream centroid detection further enables on-the-fly super-resolved event localization (Peng *et al.*, 2023).

Here we explore the advantages of leveraging fast EBEC technology, as implemented by the Apollo detector (Peng *et al.*, 2023), for small molecule MicroED. We focus on small molecule crystals since they represent a general challenge for electron counting procedures by producing fewer, more intense reflections than their macromolecular counterparts. We analyze a fluence regime that can enable high throughput data collection and determination of fast and accurate atomic structures from beam-sensitive crystals in semi-automated fashion.

2. Materials and methods

2.1. Samples & sample preparation

Crystal samples were obtained and prepared for MicroED analysis as follows:

1. Salen ligand: (*S*,*S*) Jacobsen's salen ligand was purchased from Sigma. The powder was dissolved in a solution composed of 1:2 dichloromethane to ethanol by volume, and the solution was left to slowly evaporate. After approximately 1 day, following drying of the solvent, thin rod-shaped crystals of a pale yellow color were observed. The population of crystals varied in size, some of suitable size (~0.5 mm long) for X-ray diffraction, but many much smaller. TEM grids were briefly dusted with crystalline powder, producing a distribution of sub-micron thick crystals suitable for MicroED. The anticipated salen ligand crystal polymorph was in space group $P2_12_12_1$, CCDC ID: 129337, with cell constants *a* 6.78 Å, *b* 18.33 Å, *c* 27.75, Å *α* 90°, *β* 90°, *γ* 90° (Yoon *et al.*, 1997).

2. Biotin: Biotin was purchased as a powder from Sigma. A saturated solution was prepared in water heated to 100 °C. The solution was allowed to slowly return to ambient temperature, during which colorless needle-shaped crystals formed. The crystal suspension was diluted tenfold in ethanol and saved for subsequent TEM sample preparation. Grids were prepared by pipetting 2 µL directly from this suspension, allowing the sample to settle on the grid for approximately 30 seconds, and then wicking off excess solvent with filter paper, leaving sub-micron thin needle-shaped crystals on the grid for microED analysis. The anticipated biotin crystal polymorph was in space group $P2_12_12_1$, CCDC ID: 1111310, with cell constants *a* 5.24 Å, *b* 10.35 Å, *c* 21.04 Å, *α* 90°, *β* 90°, *γ* 90° (DeTitta *et al.*, 1976).

3. Thiostrepton: 30 mg of commercially acquired thiostrepton was dissolved in 1.95 mL of a 24:1 chloroform:isoamyl alcohol solution. 390 µL of ethanol and 195 µL of 100% glycerol were added and mixed into the solution. The solution was allowed to slowly evaporate at ambient temperature, and after four days small tetragonal crystals had formed. The anticipated thiostrepton crystal polymorph was in space group $P4_32_12$, PDB ID: 1E9W, with cell constants *a* 26.58 Å, *b* 26.58 Å, *c* 27.44 Å, *α* 90°, *β* 90°, *γ* 90° (Bond *et al.*, 2001).

2.2. Instruments and data collection

Data were collected using a Talos F200C side-entry transmission electron microscope (Thermo-Fisher Scientific) operating at 200 keV. The microscope optics were configured to deliver a low flux parallel beam on the sample and to collect selected area electron diffraction. Specifically, we used an extractor voltage of 4150 V, a gun lens of 4, spot sizes in the range of 9–11, and a C2 aperture of 70 µm. For each configuration, a near-parallel beam was achieved by adjusting the C2 lens current to a value of ~44.8 % at spot size 11, and ~45.8 % at spot size 9, yielding a focused beam at the back focal plane of the objective lens; that plane was assumed to be coplanar with the objective aperture. These conditions yielded a beam approximately 3 µm in diameter, delivering an electron flux of ~ 0.01 $e^-/Å^2/s$ at spot size 11, 0.03 $e^-/Å^2/s$ at spot size 10, and 0.045 $e^-/Å^2/s$ at spot size 9. A 100 µm selected area aperture was used to sample from a ~1.2 µm radius circular area of the conjugate image plane. A virtual camera length of 420 mm yielded patterns that, as sampled by the Apollo detector, mapped a resolution of 0.8 Å at their edge. A camera length of 670 mm yielded patterns captured by the Apollo detector with a resolution of 1.4 Å at their edge. For comparison, data was also acquired using a Ceta-D detector mounted in line with the Apollo, on the same Talos F200C microscope; diffraction was recorded under the same beam conditions as for the Apollo. Due to the different positions of this detector relative to the specimen, a virtual camera length of 960 mm was necessary to capture patterns with a resolution of 0.8 Å at their edge. Diffraction was recorded as crystals were unidirectionally rotated at a fixed rate of speed, typically from 0.3 to 2 °/s. A standard tilt series spanned a 100-degree wedge of data, from +50 to –50 degrees. All crystals were aligned to eucentricity such that they remained within the selected area aperture during the entire tilt range.

2.3. Estimation of electron flux

Electron beam flux estimates were measured for all selected area electron diffraction settings described in methods section 2.2. First, the microscope was configured for parallel illumination. A magnification was selected such that the parallel beam filled the active area of the flu screen or the active area of the camera sensor. Electron flux was estimated from counts in a gain-corrected image of the parallel beam acquired by the Apollo. The number of electrons measured per pixel was determined from raw counts using a conversion factor of 16 counts per electron, corresponding to the value assigned to each detected event in Apollo's firmware. These values were used to determine the flux as a function of spot size, corresponding to ~ 0.01, 0.03, and 0.045 e-/Å^2/s for spot sizes 11, 10, and 9, respectively. In a second estimate, we recorded the flu screen current readout obtained when exposed to the parallel beam at each setting. These current readings (in amperes) were divided by the charge of an electron (1.602×10^{-19} C) and the size of the illuminated area (in Å^2) from each trial to achieve measures of flux density in e-/Å^2/s. These were determined as 0.0252 e-/Å^2/s for spot size 9 and 0.0147 e-/Å^2/s for spot size 10. The screen current readout at spot size 11 was below the threshold of detection and read out as 0 nA. For this report, we use flux and fluence values as measured by the Apollo detector.

2.4. Calculated estimates of electron counts and coincidence loss in diffraction experiments

Throughout this paper, units of e$^-$/pix/s always refer to the detection (output) rate on the sensor, not the incidence (input) rate since the detection rate may be lower than the incidence rate due to coincidence loss. To numerically simulate the number of incident electrons counted per pixel per second (e$^-$/pix/s) during EBEC, we assumed that each electron event impinging on the detector had the potential to activate a cluster of adjacent pixels (Supplementary Figure 1). The Apollo detector applies this same logic during event detection, by considering blocks of up to 5x5 physical pixels during centroid-based electron event registration (Supplementary Figures 1–3). When eight adjacent pixels, present side-by-side or diagonal, are simultaneously activated, a bounding box is defined with a maximum size of 5x5; the centroid of isolated signal pixels within this box is assumed to represent a single incident primary electron. Each 5x5 block of physical pixels may successfully detect multiple incident primary electrons, provided that the activated pixels from each are not adjacent.

For each block of physical pixels on the Apollo sensor, the detection time interval is 418 μs. Therefore, the maximum counting rate of any pixel in isolation is 2392 e^-/pix/s. However, because simultaneously activated adjacent pixels are assumed to represent the same incident primary electron, if one pixel is counting 2392 e^-/pix/s, its 8 adjacent pixels must necessarily be counting 0 e^-/pix/s. Therefore, the maximum average counting rate, averaged over a block of pixels is 1/9 the internal counting rate, equating to ~266 e^-/pix/s. In practice, the fraction of incident electrons that activate more than one pixel will further reduce this maximum average counting rate. For example, a detection event consisting of two adjacent activated pixels has 10 adjacent inactivated pixels. If all incident primary electrons always activated two adjacent pixels, then the maximum average counting rate would be 2392 / (2 + 10) = ~200 e^-/pix/s. Of course, since the shape and size of detection events on the sensor span a range of possibilities, the maximum average counting rate will be a weighted average of all of these possibilities, with the result no more than 266 e^-/pix/s.

To evaluate the impact of coincidence loss due to overlapping detection events from multiple incident primary electrons, we performed numerical simulations in which 9 independent arrays of virtual counts were generated sampling a random temporal distribution of electron arrival on the pixel within a one second interval, defined by an incident electron flux on a pixel. The 9 independent arrays of incident electrons simulated a cluster of adjacent pixels. Each was sampled at the internal count rate, and the coincidence of counts across all nine was assessed per second. Each coincident pair of events within a pixel or between pixels in a cluster contributed to the count of lost electrons. That process was sampled in a thousand trials, each with a random temporal distribution of electron counts per pixel (Supplementary Script 1). Averages and standard deviations were calculated and plotted for the measured e^-/pix/s and the corresponding lost count of e^-/pix/s (Figure 1, Supplementary Figures 1-3).

While the simulated data is in agreement with anticipated parameters, it is important to note that experimental measures of coincidence loss are often greater than those simulated here. This is due to many factors including the fact that non-uniform illumination can lead to local loss of electron counts due to hard limits on count rates during sensing. This is evidenced in diffraction data collected at increasing incident electron flux from dose-insensitive, well-diffracting crystals of Co(II) meso-tetraphenyl porphyrin, which we used as a diffraction standard. In that case, an approximately fourfold increase in incident flux does not result in a fourfold increase in observed diffraction counts across all measured signal pixels (Supplementary Figure 4), and a nearly 9-fold increase in flux, from ~0.01 to ~0.084 e^-/Å^2/s, showed a pronounced loss of counts at the brightest reflections. This was observed in scatterplots of counts at 0.01 e^-/Å^2/s vs higher incident flux values, and histograms of count ratios across those conditions. Based on that experiment, we elected to limit our incident flux for subsequent experiments to less than 0.05 e^-/Å^2/s.

2.5. The Apollo detector and its use for MicroED EBEC data measurements

The Apollo detector houses a monolithic active pixel sensor performing correlated double sampling, on-chip thresholding, on-chip event detection, and event encoding. The sensor is composed of 4x2 rectangular sensor segments comprising a contiguous 4096x4096 array of 8-micron pixels. The time resolution for event detection is 418 µs. Pixel readouts from the sensor are directly transferred to on-board field programmable gate arrays (FPGA) that carry out super-resolution centroid mapping, yielding super-resolved dose-fractionated movie frames with 8192x8192 virtual pixels. In these images, each counted electron is converted to a signal value of 16 per pixel. Although the Apollo sensor is capable of a maximum average counting rate of ~266 e^-/pix/s, the bandwidth of the on-board memory in the Apollo camera limits the detection rate to a maximum of ~126 million e^-/sensor segment/s, which equates to a maximum average counting rate of ~60 e^-/pix/s or a total counting rate of >1 billion e^-/s.

We note that these maximum counting rates are averaged over blocks of pixels and therefore are a straightforward limit during uniform illumination of the sensor. However, in diffraction, the illumination is highly non-uniform, with primary electrons concentrated in discrete reflections. In this case, the detected intensity of each reflection may be much higher than the counting rate limits discussed above, because pixels between reflection will have much lower detection rates. On average, the counting rate limits are still satisfied.

To record diffraction images from static crystals in electron counting mode, the Apollo detector was operated at an output dose-fractionated movie frame rate of 60 Hz, meaning that each output movie frame consists of the sum of all the events detected for ~16.7 ms. All images were gain-corrected and saved as full 8192x8192 frames. In this same mode, to facilitate electron counting for continuous rotation MicroED data collection, the detector was operated at a rate of 0.3–2 Hz, and stage rotation was configured such that each frame sampled one degree of data. The typical dataset, under our fast data collection scheme, sampled 100 ° in a single 100 frame-movie saved in MRC format; this was converted to a series of individual SMV format frames for processing. Slow rotation (0.3 °/s) data collection datasets sampled an equivalent wedge of reciprocal space, in an equivalent number of frames, but with a larger corresponding total fluence.

2.5.1. Using SerialEM for MicroED data collection

SerialEM was configured to record diffraction data on the Apollo detector using logic similar to that previously described by de la Cruz and co-workers (De La Cruz *et al.*, 2019). Briefly, three modes were configured to facilitate data collection using low-dose settings in SerialEM as follows: ‘View’ mode was used for generating montage overviews of the center working area of a grid. The typical montage was configured to sample an array of 7x7, 155x magnification images. These images were recorded with an exposure time of 0.25 s, 2x binned, yielding sufficient resolution to identify potential crystallites of interest (Supplementary Figure 5). Record mode was used to corroborate the positions of crystals identified in the grid montage overview. To achieve this, it was configured to acquire real-space images at 2500x - 4300x magnification, with the C2 lens condensed to illuminate the same area as would be sampled by a parallel beam when sampling diffraction. The selected area aperture, not under the control of SerialEM, was inserted as needed to confirm each crystal remained eucentric within its bounds throughout the entirety of the tilt range used for data collection (+/– 50 °). Search mode was configured to sample selected area diffraction as described in methods section 2.2, with a virtual camera length of 420–670 mm. In this mode, the Apollo was set to record single, 100-frame movies per dataset. Target crystal locations were identified from the montage image, confirmed in 'Record' mode, and added to the navigator. A script (Supplementary Script 2) was then used to collect continuous rotation MicroED data from consecutive target locations, stored in the navigator.

2.6. Analysis of reflection intensities in EBEC diffraction patterns

Diffraction patterns measured by the Apollo detector as 8192x8192x100 data stacks in MRC format were used to generate histograms of all counts as well as counts associated with measured reflections. Reflections were detected by bandpass filtering individual frames in a diffraction image stack and selecting all pixels that were 2 to 3 standard deviations above a designated background value. These pixels were considered in the set of all associated with reflections for subsequent counting analyses and were also used to count individual reflections via an image segmentation routine that partitioned connected sets of pixels into individual clusters; each cluster was assumed to be a single reflection. All statistics quoted for reflections in a given dataset were determined based on these subsets, and all figures displaying maximum or summed intensity diffraction patterns show this subset of selected pixels.

2.7. Reduction and processing of MicroED Data

MicroED movies collected on the Ceta-D camera were binned into frames of size 2048x2048 pixels, saved in SER file format, and then converted to SMV image stacks using the script ser2smv (Hattne *et al.*, 2015). Frames in these stacks were reduced in *XDS*, enforcing a corrected virtual camera length of 948 mm. Data were indexed first without enforcement of unit cell constants or space group symmetry to validate they were of sufficient quality for analysis, then reprocessed while enforcing the expected unit cell and space group symmetry for each compound. Reflections were integrated to 0.8 Å resolution, to match the resolution considered for reflections measured from the Apollo camera, then scaled in *XSCALE*.

EBEC MicroED movies collected on the Apollo DED were converted from MRC file format to SMV image stacks with custom scripts run on MATLAB version 2023b. During file conversion, frame sizes were reduced to 2048x2048 pixels, and a value of 1 was added uniformly to every pixel in each frame to avoid pixel values of 0 in the SMV images. Data collected using a virtual camera length of 420 mm was processed in *XDS* enforcing a corrected detector distance of 540 mm. Thiostrepton data collected using a virtual camera length of 670 mm were processed using a corrected detector distance of 860 mm. Data were again indexed first without enforcement of unit cell constants or space group symmetry to validate that it was of sufficient quality for analysis, then reprocessed while enforcing the expected unit cell and space group symmetry for each compound. For salen ligand and biotin crystals, reflections were integrated to a resolution of 0.8 Å, then scaled in *XSCALE.* For thiostrepton crystals, reflections were integrated to a resolution of 1.5–2.0 Å, then scaled as previously described. All data reduction statistics are reported as generated by *XSCALE*.

2.8. Coincidence loss intensity adjustment and processing of EBEC MicroED data

We sought to determine whether a CL adjustment would improve EBEC data. We calculated the mean loss of electrons for a given rate of measured counts in e^-/pix/s (Figure 1) and systematically added these counts to every pixel that measured between 10 and 260 e^-/s in diffraction frames. Electron counts were deduced from raw, gain-corrected intensity values as previously described, assuming a conversion factor of 16 counts per electron, and normalizing for the integration time per frame; where frames were typically recorded at a rate of 2 Hz or 0.3 Hz. In this scheme, a pixel with a measured count of 10 e^-/s received < 0.2 additional e^-/s, while ~25 e^-/s were added to pixels with a measured count of 100 e^-/s (Supplementary Figure 3). These values are conservative, given that real CL percentages are likely higher in experimental data, as indicated by Nakane et al (Nakane *et al.*, 2020). This addition of electron counts was systematically performed for each of the 8192x8192 pixels in all 100 raw, super-resolution diffraction images of an EBEC MicroED dataset. The counts-adjusted images were once again saved in MRC format for subsequent processing (Supplementary Script 3). CL-adjusted diffraction movies were converted into individual SMV frames as previously described, and used for subsequent data reduction in XDS.

2.9. Structure determination and refinement

Ab initio phasing of salen ligand and biotin structures was performed using SHELXD or SHELXT from HKL files reduced by XDS (Sheldrick, 2008). The resulting atomic coordinates were then further refined in ShelXLE (Hübschle *et al.*, 2011; Sheldrick, 2015) as follows: Structures obtained from SHELXD/SHELXT were refined with a WGHT parameter of 0.2 over batches of 1000 cycles of least-squares refinement until the R-factors converged, using electron scattering factors parameterized as four gaussians for each element (Saha *et al.*, 2022). Missing non-hydrogen atoms were assigned guided by Q-peaks in ShelXLE. Hydrogen atoms were placed when evident in the F_o-F_c map and Q-Peaks, and when appropriate based on likely molecular geometry, but were omitted during refinement for the purposes of comparison between datasets. All refinements were performed treating B-factors as isotropic. For each sample, representative structures were determined with riding hydrogens and anisotropic B-factor refinement whenever doing so did not result in non-positive definite (NPD) B-factors on any atoms (Figure 2). Structures of thiostrepton were determined by molecular replacement using *MOLREP* with PDB entry 1E9W as a search model and refined in PHENIX. Bond length restraints of 1.7 Å +/- 0.02 Å were implemented for all five thiazole sulfur atoms and their neighboring backbone carbon atoms to keep the thiazole rings intact during cycles of refinement. Planarity restraints with a standard deviation of 0.005 Å were also applied over each atom in an *sp*^{2} hybridization environment on the thiazole rings of the thiostrepton molecule. For each thiostrepton dataset used for structure determination, molecular replacement in *MOLREP* was also performed using the model from PDB entry 1E9W with all residues mutated to alanine (Vagin & Teplyakov, 1997), followed by a cycle of rigid body refinement in *PHENIX* (Adams *et al.*, 2010), to visualize Fourier difference maps to reveal density for atoms not supplied in the search model. Isotropic B-factors were refined over residues. Structures were visualized in Coot and rendered in PyMol. Ortep diagrams were generated in ORTEP-3 (Farrugia, 1997) using CIF files generated from SHELX refinement.

3. Results

3.1. Coincidence loss estimates when applying fast EBEC to electron diffraction

Coincidence loss presents a major challenge for electron counting since it reduces the linearity of the sensor response and decreases the effective dynamic range achievable by that sensor. In diffraction measurements, the undercounting of coincident electrons decreases signal at bright reflections, leading to inaccurate integration of intensities. While single-particle imaging experiments can rely on a relatively constant illumination profile on the detector for estimates of coincidence, one cannot readily determine the anticipated degree of non-zero coincidence at a given Bragg reflection by simply knowing the incident flux on the crystal being diffracted. This makes it imperative to anticipate the degree of CL expected at any given pixel under any possible electron flux at that pixel.

The likelihood of zero coincidence can be estimated for a single pixel in a counting detector. For a given count rate M and flux N, this can be estimated by $P(M,N) = [M!/(N!(M-N)!)](1/M^N)$, for $M>N$. The probability indicates that deviations from zero coincidence would be expected despite high count rates and low flux values, requiring careful consideration of the chosen flux for an experiment. This is true if each detector pixel is considered to count with full independence of all others, and more so if events across neighboring pixels are considered correlated during counting (Supplementary Figure 1). More specifically, given that each pixel on the Apollo sensor counts at a rate of 2392 e^-/pix/s, we can first consider the condition where electrons arrive only at a single pixel and it counts them independently of all other pixels on the sensor. Under these conditions, a 3% CL is expected when detecting a true incident flux of 100 e^-/pix/s; a 10% CL is expected for a true incident flux of 500 e^-/pix/s (Supplementary Figure 2). However, in a more realistic scenario, each electron strikes a cluster of pixels on the sensor, and counts are assessed from 3x3 patches of pixels on the sensor. Then, simulations indicate a lower bound of ~18% CL is anticipated for an incident flux of 100 e^-/pix/s, and > 50% CL is expected for an incident flux of 500 e^-/pix/s (Supplementary Figure 3).

Correlation between adjacent pixels during counting means the Apollo, with an internal count rate of 2392 e$^-$/pix/s, has an effective counting rate of ~266 e$^-$/pix/s. Given that effective count rate, a true incident flux of 96 e$^-$/s on a pixel would result in only ~80 e$^-$/s being counted (Figure 1). Conversely, if less than 80 e$^-$/pix/s are detected, CL is expected to be lower than 20 %. For example, if 10 e-/pix/s are detected, an average loss of less than 1 e$^-$/pix/s is expected (Figure 1). These calculations set important bounds for signal counts at reflections and ultimately, for incident beam flux on a crystal. When diffracting from small molecule crystals, we therefore targeted a maximum measured count rate of 80 e$^-$/pix/s and set out to define experimental conditions yielding reflection counts that obeyed this limit when diffracting from salen ligand, biotin, and thiostrepton crystals (Figure 1).

3.2. The impact of electron beam flux on fast EBEC for small molecule electron diffraction

To assess the degree of CL observed in EBEC MicroED patterns, we initially recorded diffraction from 6 salen crystals at increasing values of incident electron beam flux on the crystal: ~0.01, 0.03, and 0.045 e$^-$/Å^2/s (Supplementary Figure 6). We chose salen ligand crystals since their unit cell, morphology and degree of order were characteristic of the type of organic small molecule microcrystals that might yield *ab initio* structures by MicroED. We recorded one second-long, 60-frame movies under these conditions, noting that the illuminated crystals were stable and did not suffer any radiation-induced decay in diffraction signal during that exposure. Electron count distributions from all measured reflections detected in second-long movies from various crystals showed maximum counts ranging from 71 to 206 e$^-$/pix/s for an incident flux of 0.01 e$^-$/Å^2/s, and maximum counts ranging from 8 to 246 e$^-$/pix/s for the highest incident flux of 0.045 e$^-$/Å^2/s (Supplementary Figure 6, Supplementary Table 1). These measurements underscored the uncertainty of maximal electron counts at reflections as a function of incident beam flux on a crystal, which is affected by shot noise. However, the fraction of pixels in measured reflections that exceeded 80 e$^-$/pix/s more closely mirrored the changes in incident beam flux (Supplementary Table 1). This inspired a further analysis of CL and its impact on MicroED data quality.

We assessed the impact of EBEC data collection on the overall quality of MicroED data collected with settings typically used for small molecule *ab initio* structure determination (Supplementary Figures 7–9). To assess the quality of EBEC data with respect to conventional datasets, we directly compared diffraction from salen ligand crystals, measured using either the scintillator-based CMOS-based camera (CETA-D) or the Apollo detector. Diffraction movies were recorded with both the CETA-D and the Apollo from individual salen ligand crystals with an incident electron beam flux of 0.01 and 0.045 e$^-$/Å^2/s. EBEC data showed improved contrast and signal-to-noise (Supplementary Figures 7–9), but, under these conditions, a large fraction of measured pixels in EBEC patterns had counts in the range of 10–80 e-/pix/s, where some CL might be expected (Supplementary Figure 9).

3.3. The impact of fast EBEC on the quality of small molecule MicroED datasets.

To determine whether the CL observed during fast EBEC data collection would impact structure determination, we analyzed data under varying illuminating beam fluence from crystals of our three candidate molecules: the salen ligand, biotin, and thiostrepton. For all three samples, we cataloged the counts of e^-/s for every pixel in each of the hundred frames of a measured dataset (Figure 2, Supplementary Figures 10–15). Distributions of electron counts showed that the majority of pixels received only a few e^-/s, including at our highest chosen illuminating beam flux of 0.045 $e^-/Å^2/s$ (Figures 1–2). Low counts were generally observed, even from salen ligand crystals, the strongest diffracting and most robust of our chosen samples (Figures 1–2, Supplementary Figures 10–11). However, in some high flux (0.045 $e^-/Å^2/s$) salen ligand datasets, as many as 0.03% of pixels in a given diffraction frame had counts above 80 e^-/pix/s (Supplementary Figure 11). By comparison, salen ligand diffraction collected at our lowest chosen flux of 0.01 $e^-/Å^2/s$ had fewer pixels with signal above this threshold (Supplementary Figure 11).

Equivalent count distributions were observed for biotin crystal reflections (Figures 1–2, Supplementary Figures 12–13), although some of those reflections still registered electron counts above the 80 e^-/pix/s threshold (Supplementary Figures 12–13). In contrast, under equivalent conditions, thiostrepton crystals did not diffract as brightly or to atomic resolution; they consistently yielded ~1.5–2 Å datasets even at the highest incident beam flux. Counts in thiostrepton crystal data were also on average 2–5 times lower than those from biotin or salen ligand crystals and rarely exceeded 80 e^-/pix/s (Figures 1–2 and Supplementary Figures 14–15). Those counts are consistent with the comparatively lower total number of illuminated unit cells and overall lower diffraction quality of thiostrepton crystals.

Reasoning that a CL-induced reduction of the dynamic range of measured intensities might be detected as pseudo-twinning, we charted data reduction statistics and, in particular, the twinning-indicator L-test result for EBEC MicroED data (Supplementary Figures 16–17). All crystals rotated at 0.3 °/s had estimated twin fractions of 0. In contrast, more quickly rotating salen ligand and biotin crystals had L-statistic-derived estimated twin fractions that, while low, were greater than zero on average (Supplementary Table 3). This indicated that fast EBEC sampled from strongly diffracting crystals might suffer a mild degree of CL that can be registered by twin tests (Supplementary Figure 17).

3.4. Leveraging fast EBEC for low-dose MicroED structures of beam-sensitive organic small molecules

We evaluated the ability to determine accurate structures of small molecules from EBEC MicroED data collected using an incident electron beam flux of only 0.01 $e^-/Å^2/s$. This flux yielded high-quality datasets from all sampled crystals; data were sufficiently accurate and complete to yield *ab initio* structures from salen ligand and biotin crystals (Figure 3, Tables 1, 2). Preliminary solutions from salen ligand datasets recorded under these conditions contained 40 accurately placed atoms that could be further refined to structures with an average R_1/R_{wall} of 0.2689/0.2928 and average GooF of

1.989 and showed clear density for 2 H-atoms (Figure 3). Similarly, preliminary solutions obtained from biotin crystals showed 16 atoms and could be further refined structures with an average R_1/R_{wall} of 0.2873/0.3244 and average GooF of 1.590; these also showed clear density for 2 H-atoms (Figure 3). Datasets that could not be stably refined using SHELXLE had R_1 statistics well exceeding 50 % and were not included in subsequent analyses (Figure 4).

Data from thiostrepton crystals failed to reach atomic resolution but were sufficient for molecular replacement (Figure 3, Table 3). Solutions could be achieved using *MOLREP* for datasets acquired from thiostrepton under all three fluence conditions, but subsequent refinement was most successful for crystals exposed to the highest fluence of 3.33 $e^-/Å^2$. Structures determined under these conditions could be refined to R_{work}/R_{free} of 0.2433/0.2488, had an overall B-factor of 11.04 $Å^2$, and showed fully intact side chain density for 6 residues, including all five thiazole rings on the molecule. Data collected at the lowest fluence (0.5 $e^-/Å^2$) was not generally suitable for high-quality refinement but was still sufficient to visualize the most ordered core of the molecule. In these refinements, side chain density was visible in Fourier difference maps resulting from the refinement of the data against poly-alanine models of thiostrepton (Figure 3, Supplementary Table 2).

3.5. A coincidence loss adjustment for EBEC-mediated MicroED and its impact on the accuracy of small molecule structures

To determine the potential benefit to be gained from reduced CL in fast EBEC MicroED data, we used the known counting rate of the Apollo detector and measured electron counts per second for any given pixel to implement a simple CL adjustment. While limited, we hoped the adjustment might approximate closer to true counts from measured values and indicate whether more refined adjustments would be beneficial. The adjustment is determined from estimates of the number of undercounted electrons from numerical simulations (Figure 1, Supplementary Figures 1–3). As the rate of incoming electrons increases, the number of counts detected per unit time asymptotically approaches the effective maximum count rate per pixel. We estimate that, for the Apollo, this value should be ~266 e^-/pix/s. Based on this rate, numerical calculations would suggest that 80 counted e^-/pix/s should be adjusted to ~96 e^-/pix/s, to account for CL. Although an ~2 e^-/pix/s standard deviation is associated with this correction, that degree of uncertainty is lower than the magnitude of the error due to potentially lost counts (Figure 1, Supplementary Figure 3). These calculated adjustments were applied to raw measured pixel counts, creating CL-adjusted datasets with increased electron counts.

We applied the CL adjustment to all our EBEC MicroED datasets. We found that in fast EBEC diffraction patterns measured from salen ligand crystals illuminated with a flux of 0.045 $e^-/Å^2/s$, approximately 0.003 % of all pixels had counts > 80 e^-/pix/s (Supplementary Figures 10-11). Despite the low number of pixels affected, those pixels were distributed across a wide number of frames and reflections. Some affected pixels had counts that approached the effective counting limit of the sensor

(Supplementary Figures 10–11); these were principally observed in high-incident beam flux datasets. In contrast, data from crystals illuminated with the lowest beam flux had few or no pixels above this threshold. These trends were also displayed by data collected from biotin crystals (Supplementary Figures 12–13) and, to a far lesser degree, thiostrepton crystals, which diffracted weakly regardless of incident beam flux (Supplementary Figures 14–15).

To determine the potential impact of these CL-affected pixels on data reduction and structure determination, we compared raw, unmodified diffraction intensities to their CL-adjusted counterparts. Data reduction parameters optimized for raw, un-adjusted diffraction frames were used unchanged for processing of their CL-adjusted counterparts. CL adjustment of diffraction frames improved their dynamic range, particularly for low-resolution reflections (Supplementary Figures 18–20). The consistency and accuracy of adjusted reflections were judged in part by data reduction statistics (Figure 4). Analysis of twin law tests for unmodified and CL-adjusted EBEC MicroED data from salen ligand and biotin crystals illuminated with low fluence showed uniformly reduced evidence of pseudo-twinning after CL adjustment, consistent with its anticipated improvement of dynamic range (Figure 4, Supplementary Table 3). However, applying the CL adjustment to higher flux (0.045 $e^{-}/Å^{2}/s$) and fluence (2.25 $e^{-}/Å^{2}$), salen ligand and biotin crystal datasets generally yielded negligible changes to the estimated twin fraction. In most of these cases, CL adjustment decreased the estimated twin fraction, albeit slightly, and only in the case of one salen ligand crystal did we observe a negligible increase in the estimated twin fraction upon applying the CL adjustment.

Using the L-test as a diagnostic of the degree of CL in MicroED data, we concluded that EBEC data collected quickly is improved by CL adjustment, but little improvement is seen for data acquired more slowly with higher total fluence. Notably, while CL adjustment did not meaningfully change R_{merge} and I/sigma, structures from CL-adjusted data generally refined to lower R_1/R_{wall} than their unadjusted counterparts (Figure 4). Overall, these metrics indicate that more robust CL adjustments might further enhance the effective dynamic range of low flux fast EBEC data and improve the quality of MicroED structures. Ultimately, a more robust and thorough CL model would be needed for universal CL adjustments.

4. Discussion and Conclusions

Electron counting is meant to allow a less obstructed view of signal close to the noise floor. However, despite its successful application to imaging in cryoEM, electron counting has been less widely adopted for MicroED. This could in part be due to CL, which can limit dynamic range. Nonetheless, a handful of structures of peptide and protein crystals have been determined by MicroED from data collected on DEDs (Gallagher-Jones *et al.*, 2020; Hattne *et al.*, 2019, 2023) in experiments engineered to reduce the likelihood of CL. However, those efforts are not expected to readily translate to accurate small molecule MicroED data collection.

We set out to (1) assess the feasibility of electron counting applied to small molecule MicroED data collection, (2) determine the potential benefit of fast EBEC for detection of accurate diffracted intensities from small molecule crystals by MicroED, and (3) evaluate the impact of CL and a CL adjustment on small molecule MicroED. Compared to the Ceta-D, the detector of record in a large fraction of the deposited MicroED structures in the PDB, EBEC data collection facilitated more rapid data acquisition, thereby yielding high-completeness single crystal diffraction datasets that were less impacted by beam-induced radiolytic damage. Attempts to acquire data as rapidly using the Ceta-D, matching the stage rotation speed (2 °/s) and frame rate (2 frames/s) used in the fast EBEC experiments, yielded data with inferior reduction statistics. In particular, for data collected on the salen ligand with an incident beam flux of 0.01 e^-/Å/s and fast rotation of 2 °/s, overall R_{merge} statistics from these Ceta-D datasets were more than double what was achieved with fast EBEC (Supplementary Table 4). For this comparison, overall I/sigma statistics were twice better using fast EBEC. That discrepancy was less dramatic when the same comparison was made with a higher incident beam flux of 0.045 e^-/Å/s (Supplementary Table 5). Nonetheless, statistics from fast EBEC data were preferable in all cases.

High-quality fast EBEC data showed some degree of CL, but were sufficient for accurate *ab initio* structure determination by MicroED. Not surprisingly, the greatest dynamic range was observed under the highest beam fluence, granted by extended data collection times. Most importantly, however, accurate structures could be determined from fast rotation data with higher beam flux, where the measured electron counts were overall higher. Ultimately, optimizing the quality of diffraction movies involved balancing incident flux and speed of data collection to yield the greatest dynamic range in accurately measured intensities. Although considerable CL is expected for the pixels with measured counts approaching the effective count rate of the Apollo (~266 e^-/pix/s), we also note that this assumed count rate depends on the uniform propensity for electrons to impact pixels on a sensor. A higher count rate could be possible if that likelihood were skewed. This would be the case, for example, where a train of electrons only impinges on a single pixel and never its neighbors, a condition that may be present at Bragg reflections.

A higher dynamic range can potentially be achieved with longer or multiple exposures, but such detection strategies can increase the dose on target crystals. Alternatively, numerical estimates of CL can allow for adjustments that compensate for lost electrons to further enhance the dynamic range of measured diffraction patterns *ex post facto*. We found such an adjustment to slightly improve MicroED data collected from salen ligand and biotin crystals. Given the characteristics of these crystals, improved CL adjustments could generally improve EBEC MicroED data collected from small molecule crystals. DEDs could also fully overcome electron counting limitations by operating at substantially faster readout rates. For example, the readout of pixels in a detector operating at many kilohertz, as is achieved by the 4D Camera, would dramatically reduce CL, but would also produce large volumes of information to be handled *ex post facto* (Ercius *et al.*, 2023). Collectively, our experiments indicate that current fast

EBEC approaches are sufficient for the determination of accurate *ab initio* structures by MicroED, with future speed improvements and CL adjustments continuing to reduce CL and improve data quality.

Conclusion

With the growing interest in applying DEDs to diffraction measurements, the use of fast EBEC strategies offers advantages for MicroED data collection. We find that these tools enable the determination of accurate atomic structures of organic small molecules with electron fluences as low as 0.5 $e^-/Å^2$. Although CL is expected in EBEC data, the count rates observed under low flux conditions suggest only a small fraction of diffracted intensities suffer significant losses. Further, a CL adjustment to measured electron counts can take into account anticipated losses of electron counts and enhance dynamic range. Importantly, fast EBEC expedites the determination of accurate structures from beam-sensitive biomolecules such as biotin, without imposing added labor or time to data collection. This is further facilitated by the compatibility of new DEDs, such as the Apollo, with semi-automated data collection tools, such as SerialEM. Finally, by reducing the need for sampling and combining data from large numbers of crystals, fast EBEC further expands access to structures from rare beam-sensitive crystals, polymorphs, or trace impurities.

Acknowledgements We thank Drs. Michael Sawaya (UCLA) and Ambarneil Saha (LBNL) for their input and helpful discussions. We especially thank Isabel Hernandez Rodriguez (Caltech) for her technical input on electron diffraction automation. We also thank Dr. Benjamin Bammes (DE) for his technical guidance on the Direct Electron Apollo camera and helpful discussions on coincidence loss estimation. This work was supported by DOE Grant DE-FC02-02ER63421 and NIH-NIGMS Grant R35 GM128867. J.A.R. is supported as a Packard Fellow. This work is also funded by the HHMI Emerging Pathogens Initiative. Structures determined from Apollo data of the salen ligand and biotin are deposited under CCDC deposition numbers 2370186 (salen ligand) and 2370185 (biotin), respectively, and a structure of thiostrepton is deposited under PDB accession code 9CQ0. Diffraction data are available under Zenodo entries 13690162, 13713098, 13716076, and 13716389.

Author Contributions: N.V, H.M.N. and J.A.R. designed and guided experiments. N.V. and J.A.R. prepared and characterized samples. N.V., S.Q, L.S.R., L.S.M., D.C. and J.A.R. measured and analyzed diffraction data. N.V., S.Q and L.S.R. determined and refined structures. All authors helped write and provided critical feedback on the article.

References

Adams, P. D., Afonine, P. V., Bunkóczi, G., Chen, V. B., Davis, I. W., Echols, N., Headd, J. J., Hung, L.-W., Kapral, G. J., Grosse-Kunstleve, R. W., McCoy, A. J., Moriarty, N. W., Oeffner, R., Read, R. J., Richardson, D. C., Richardson, J. S., Terwilliger, T. C. & Zwart, P. H. (2010). *Acta Crystallogr D Biol Crystallogr* **66**, 213–221.

Bond, C. S., Shaw, M. P., Alphey, M. S. & Hunter, W. N. (2001). *Acta Crystallogr D Biol Crystallogr* **57**, 755–758.

Brázda, P., Palatinus, L. & Babor, M. (2019). *Science* **364**, 667–669.

Bücker, R., Hogan-Lamarre, P., Mehrabi, P., Schulz, E. C., Bultema, L. A., Gevorkov, Y., Brehm, W., Yefanov, O., Oberthür, D., Kassier, G. H. & Dwayne Miller, R. J. (2020). *Nat Commun* **11**, 996.

Clabbers, M. T. B., Martynowycz, M. W., Hattne, J. & Gonen, T. (2022). *Journal of Structural Biology: X* **6**, 100078.

Clabbers, M. T. B., Martynowycz, M. W., Hattne, J., Nannenga, B. L. & Gonen, T. (2022). *Journal of Structural Biology* **214**, 107886.

De La Cruz, M. J., Martynowycz, M. W., Hattne, J. & Gonen, T. (2019). *Ultramicroscopy* **201**, 77–80.

Delgadillo, D. A., Burch, J. E., Kim, L. J., De Moraes, L. S., Niwa, K., Williams, J., Tang, M. J., Lavallo, V. G., Khatri Chhetri, B., Jones, C. G., Rodriguez, I. H., Signore, J. A., Marquez, L., Bhanushali, R., Woo, S., Kubanek, J., Quave, C., Tang, Y. & Nelson, H. M. (2024). *ACS Cent. Sci.* **10**, 176–183.

DeTitta, G. T., Edmonds, J. W., Stallings, W. & Donohue, J. (1976). *J. Am. Chem. Soc.* **98**, 1920–1926.

Dolomanov, O. V., Bourhis, L. J., Gildea, R. J., Howard, J. A. K. & Puschmann, H. (2009). *J Appl Crystallogr* **42**, 339–341.

Duyvesteyn, H. M. E., Kotecha, A., Ginn, H. M., Hecksel, C. W., Beale, E. V., De Haas, F., Evans, G., Zhang, P., Chiu, W. & Stuart, D. I. (2018). *Proc. Natl. Acad. Sci. U.S.A.* **115**, 9569–9573.

Emsley, P. & Cowtan, K. (2004). *Acta Crystallogr D Biol Crystallogr* **60**, 2126–2132.

Ercius, P., Johnson, I. J., Pelz, P., Savitzky, B. H., Hughes, L., Brown, H. G., Zeltmann, S. E., Hsu, S.-L., Pedroso, C. C. S., Cohen, B. E., Ramesh, R., Paul, D., Joseph, J. M., Stezelberger, T., Czarnik, C., Lent, M., Fong, E., Ciston, J., Scott, M. C., Ophus, C., Minor, A. M. & Denes, and P. (2023). https://doi.org/10.48550/ARXIV.2305.11961.

Farrugia, L. J. (1997). *J Appl Crystallogr* **30**, 565–565.

Gallagher-Jones, M., Bustillo, K. C., Ophus, C., Richards, L. S., Ciston, J., Lee, S., Minor, A. M. & Rodriguez, J. A. (2020). *IUCrJ* **7**, 490–499.

Gallagher-Jones, M., Ophus, C., Bustillo, K. C., Boyer, D. R., Panova, O., Glynn, C., Zee, C.-T., Ciston, J., Mancia, K. C., Minor, A. M. & Rodriguez, J. A. (2019). *Commun Biol* **2**, 26.

Hattne, J., Clabbers, M. T. B., Martynowycz, M. W. & Gonen, T. (2023). *Structure* **31**, 1504-1509.e1.

Hattne, J., Martynowycz, M. W., Penczek, P. A. & Gonen, T. (2019). *IUCrJ* **6**, 921–926.

Hattne, J., Reyes, F. E., Nannenga, B. L., Shi, D., De La Cruz, M. J., Leslie, A. G. W. & Gonen, T. (2015). *Acta Crystallogr A Found Adv* **71**, 353–360.

Hogan-Lamarre, P., Luo, Y., Bücker, R., Miller, R. J. D. & Zou, X. (2024). *IUCrJ* **11**, 62–72.

Hübschle, C. B., Sheldrick, G. M. & Dittrich, B. (2011). *J Appl Crystallogr* **44**, 1281–1284.

Jones, C. G., Martynowycz, M. W., Hattne, J., Fulton, T. J., Stoltz, B. M., Rodriguez, J. A., Nelson, H. M. & Gonen, T. (2018). *ACS Cent. Sci.* **4**, 1587–1592.

Kabsch, W. (2010). *Acta Crystallogr D Biol Crystallogr* **66**, 125–132.

Li, X., Zheng, S. Q., Egami, K., Agard, D. A. & Cheng, Y. (2013). *Journal of Structural Biology* **184**, 251–260.

Martynowycz, M. W., Clabbers, M. T. B., Hattne, J. & Gonen, T. (2022). *Nat Methods* **19**, 724–729.

Martynowycz, M. W., Zhao, W., Hattne, J., Jensen, G. J. & Gonen, T. (2019). *Structure* **27**, 545-548.e2.

McMullan, G., Faruqi, A. R., Clare, D. & Henderson, R. (2014). *Ultramicroscopy* **147**, 156–163.

Murshudov, G. N., Skubák, P., Lebedev, A. A., Pannu, N. S., Steiner, R. A., Nicholls, R. A., Winn, M. D., Long, F. & Vagin, A. A. (2011). *Acta Crystallogr D Biol Crystallogr* **67**, 355–367.

Nakane, T., Kotecha, A., Sente, A., McMullan, G., Masiulis, S., Brown, P. M. G. E., Grigoras, I. T., Malinauskaite, L., Malinauskas, T., Miehling, J., Uchański, T., Yu, L., Karia, D., Pechnikova, E. V., De Jong, E., Keizer, J., Bischoff, M., McCormack, J., Tiemeijer, P., Hardwick, S. W., Chirgadze, D. Y., Murshudov, G., Aricescu, A. R. & Scheres, S. H. W. (2020). *Nature* **587**, 152–156.

Palatinus, L., Brázda, P., Boullay, P., Perez, O., Klementová, M., Petit, S., Eigner, V., Zaarour, M. & Mintova, S. (2017). *Science* **355**, 166–169.

Parkhurst, J. M., Crawshaw, A. D., Siebert, C. A., Dumoux, M., Owen, C. D., Nunes, P., Waterman, D., Glen, T., Stuart, D. I., Naismith, J. H. & Evans, G. (2023). *IUCrJ* **10**, 270–287.

Peng, R., Fu, X., Mendez, J. H., Randolph, P. S., Bammes, B. E. & Stagg, S. M. (2023). *Journal of Structural Biology: X* **7**, 100080.

Rodriguez, J. A., Eisenberg, D. S. & Gonen, T. (2017). *Current Opinion in Structural Biology* **46**, 79–86.

Rodriguez, J. A., Ivanova, M. I., Sawaya, M. R., Cascio, D., Reyes, F. E., Shi, D., Sangwan, S., Guenther, E. L., Johnson, L. M., Zhang, M., Jiang, L., Arbing, M. A., Nannenga, B. L., Hattne, J., Whitelegge, J., Brewster, A. S., Messerschmidt, M., Boutet, S., Sauter, N. K., Gonen, T. & Eisenberg, D. S. (2015). *Nature* **525**, 486–490.

Saha, A., Nia, S. S. & Rodríguez, J. A. (2022). *Chem. Rev.* **122**, 13883–13914.

Saha, A., Pattison, A., Mecklenburg, M., Brewster, A., Ercius, P. & Rodriguez, J. A. (2023). *Microscopy and Microanalysis* **29**, 309–310.

Sheldrick, G. M. (2008). *Acta Crystallogr A Found Crystallogr* **64**, 112–122.

Sheldrick, G. M. (2015). *Acta Crystallogr C Struct Chem* **71**, 3–8.

Shi, D., Nannenga, B. L., Iadanza, M. G. & Gonen, T. (2013). *eLife* **2**, e01345.

Takaba, K., Maki-Yonekura, S., Inoue, S., Hasegawa, T. & Yonekura, K. (2021). *Front. Mol. Biosci.* **7**, 612226.

Vagin, A. & Teplyakov, A. (1997). *J Appl Crystallogr* **30**, 1022–1025.

Wang, Y., Yang, T., Xu, H., Zou, X. & Wan, W. (2018). *J Appl Crystallogr* **51**, 1094–1101.

Winter, G., Waterman, D. G., Parkhurst, J. M., Brewster, A. S., Gildea, R. J., Gerstel, M., Fuentes-Montero, L., Vollmar, M., Michels-Clark, T., Young, I. D., Sauter, N. K. & Evans, G. (2018). *Acta Crystallogr D Struct Biol* **74**, 85–97.

Wu, S., Armache, J.-P. & Cheng, Y. (2016). *Microscopy (Tokyo)* **65**, 35–41.

Yoon, J. W., Yoon, T.-S. & Shin, W. (1997). *Acta Crystallogr C Cryst Struct Commun* **53**, 1685–1687.

Zhao, J., Xu, H., Lebrette, H., Carroni, M., Taberman, H., Högbom, M. & Zou, X. (2021). *Nat Commun* **12**, 5036.

Table 1 Structures from single salen ligand crystals

Detector	Apollo	Apollo	Apollo
Frame rate (Hz)	2	0.3	2
Data Collection and Processing			
Stage rotation rate (°/s)	2	0.3	2
Data collection time (s)	50	333	50
Electron Flux (e^-/Å^2/s)	0.01	0.01	0.045
Total Fluence (e^-/Å^2)	0.5	3.33	2.25
Resolution (Å)	20 – 0.8 (0.9-0.8)	20 – 0.8 (0.9-0.8)	20 – 0.8 (0.9-0.8)
Space Group	$P2_12_12_1$	$P2_12_12_1$	$P2_12_12_1$
a, *b*, *c* (Å)	6.62, 17.84, 27.37	6.66, 18.12, 27.51	6.64, 18.06, 27.33
α, *β*, *γ* (°)	90,90,90	90,90,90	90,90,90
# total reflections	13477 (3656)	13789 (3838)	13550 (3818)
# unique reflections	2788 (801)	3215 (928)	3079 (879)
R_{merge} (%)	15.40 (34.70)	10.70 (149.50)	14.50 (83.00)
CC1/2 (%)	99.1 (47.9)	99.5 (33.2)	99.1 (51.5)
<I/σI>	6.08 (3.97)	5.34 (0.74)	6.02 (1.46)
Completeness (%)	74.0 (74.1)	82.9 (82.9)	80.5 (80.6)
Phasing			
N trials	50000	50000	50000
N trials with CFOM > 80	2310	3810	3451
Refinement			
Resolution (Å)	20 – 0.8 (0.9-0.8)	20 – 0.8 (0.9-0.8)	20 – 0.8 (0.9-0.8)
R_1 / $R1_{all}$ (%)	20.82/ 24.32	11.67 / 17.07	11.75 / 15.51
wR2 (%)	51.75	36.41	36.46
GooF	1.684	1.053	1.150
# atoms placed by SHELXD	40	40	40
# H-atoms seen in Fo-Fc map	4	2	0

Table 2 Structures from single biotin crystals

Detector	Apollo	Apollo	Apollo
Frame rate (Hz)	2	0.3	2
Data Collection and Processing			
Stage rotation rate (°/s)	2	0.3	2
Data collection time (s)	50	333	50
Electron Flux ($e^-/Å^2/s$)	0.01	0.01	0.045
Total Fluence ($e^-/Å^2$)	0.5	3.33	2.25
Resolution (Å)	20 – 0.8 (0.9-0.8)	20 – 0.8 (0.9-0.8)	20 – 0.8 (0.9-0.8)
Space Group	$P2_12_12_1$	$P2_12_12_1$	$P2_12_12_1$
a, *b*, *c* (Å)	5.12, 10.15, 20.56	5.11, 10.18, 20.76	5.09, 10.08, 20.65
α, *β*, *γ* (°)	90,90,90	90,90,90	90,90,90
# total reflections	4456 (1220)	4422 (1184)	2840 (782)
# unique reflections	1265 (359)	1126 (324)	1024 (367)
R_{merge} (%)	15.3 (26.9)	14.6 (45.4)	11.9 (28.2)
CC1/2 (%)	97.5 (67.5)	99.0 (77.5)	97.8 (86.3)
<I/σI>	5.92 (4.25)	5.66 (2.53)	5.55 (2.83)
Completeness (%)	95.0 (95.7)	85.3 (86.9)	79.0 (80.1)
Phasing			
Best SHELXT CFOM	0.5389	0.6603	0.7221
N trials (SHELXT)	6400	6400	6400
N trials (SHELXD)	50000	50000	50000
N trials with CFOM > 80 (SHELXD)	7616	7693	265
Refinement			
Resolution (Å)	20 – 0.8 (0.9-0.8)	20 – 0.8 (0.9-0.8)	20 – 0.8 (0.9-0.8)
R_1 / $R1_{all}$ (%)	17.88 / 22.43	15.86 / 18.56	19.42 / 21.05
wR_2 (%)	48.78	40.94	50.02
GooF	1.626	1.325	1.652
# atoms placed by SHELXT	16	16	16
# H-atoms seen in Fo-Fc map	2	1	4

Table 3 Structures from single thiostrepton crystals

Detector	Apollo	Apollo	Apollo
Frame rate (Hz)	2	0.3	2
Data Collection and Processing			
Stage rotation rate (°/s)	2	0.3	2
Data collection time (s)	50	333	50
Electron Flux ($e^-/Å^2/s$)	0.01	0.01	0.045
Total Fluence ($e^-/Å^2$)	0.5	3.33	2.25
Resolution (Å)	19.09 – 2.0 (2.1-2.0)	18.72 – 1.5 (1.6 – 1.5)	15.56 – 1.81 (1.9-1.81)
Space Group	$P4_32_12$	$P4_32_12$	$P4_32_12$
a, b, c (Å)	27.00, 27.00, 27.51	26.47, 26.47, 27.29	26.68, 26.68. 27.52
α, β, γ (°)	90,90,90	90,90,90	90,90,90
# total reflections	4938	12605 (2143)	5437 (761)
# unique reflections	717 (88)	1738 (289)	969 (129)
R_{merge} (%)	27.0 (82.4)	20.4 (117.8)	24.7 (66.6)
CC1/2 (%)	98.6 (67.1)	98.5 (57.2)	98.3 (60.1)
<I/σI>	5.41 (2.61)	6.67 (1.89)	5.46 (2.51)
Completeness (%)	88.2 (83.0)	99.3 (98.6)	91.2 (88.4)
Phasing			
Search model PDB	1E9W	1E9W	1E9W
Refinement			
Resolution (Å)	19.09 – 2.0	18.72 - 1.50	15.56 – 1.81
R_{work} (%)	21.89	20.26	23.37
R_{free} (%)	29.39	21.67	30.19
# protein atoms	118	118	118
# solvent molecules	1	2	1
Average B-factor	11.07	13.09	13.83

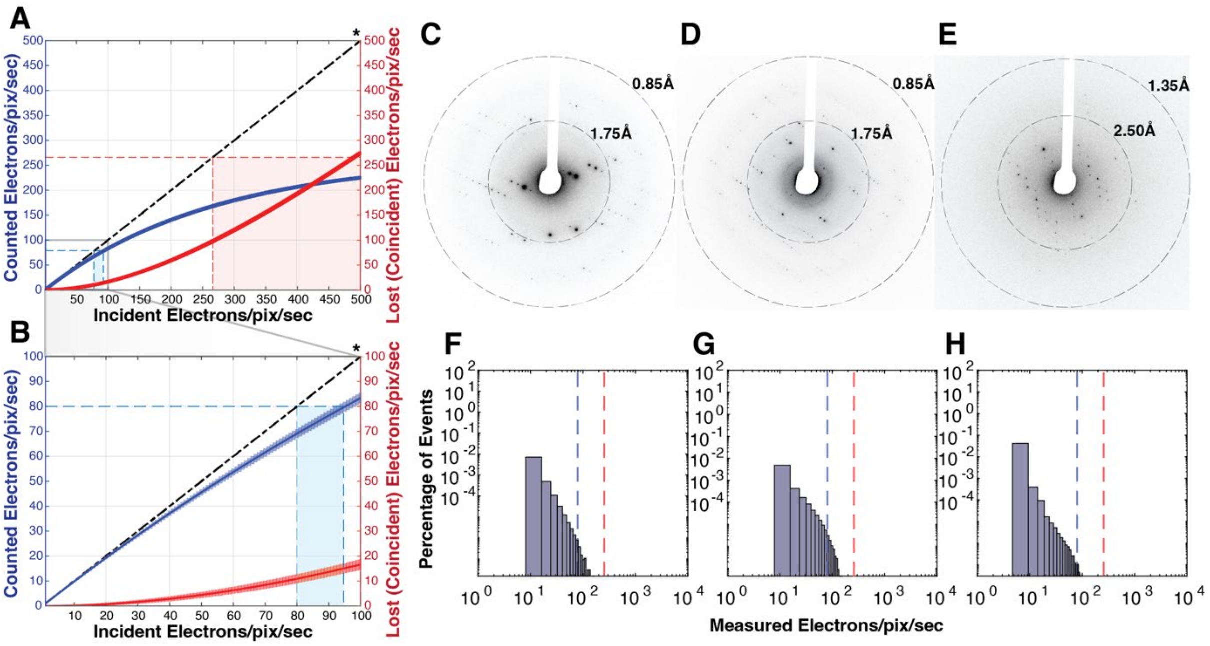

Figure 1 Analysis of EBEC diffraction data as a function of incident electron flux. (A) Simulated estimates of anticipated CL as a function of electron flux incident on a given detector pixel. Inset (B) magnifies the region from 0 to 100 e^{-}/pix/s in (A). A star denotes the hypothetical line corresponding to perfect counting. The maximum internal count rate for the Apollo detector is denoted in bold: 2,392 e^{-}/pix/s. EBEC diffraction patterns from salen ligand crystals (C), biotin crystals (D), and thiostrepton crystals (E) were collected with an incident flux of 0.045 e^{-}/Å^{2}/s on each crystal; resolution rings are marked with dashed lines. Measured electron count distributions in EBEC MicroED datasets collected from crystals of the salen ligand (F), biotin (G), and thiostrepton (H) at the same incident flux are shown. Distributions tabulate all registered e^{-}/pix/s greater than zero.

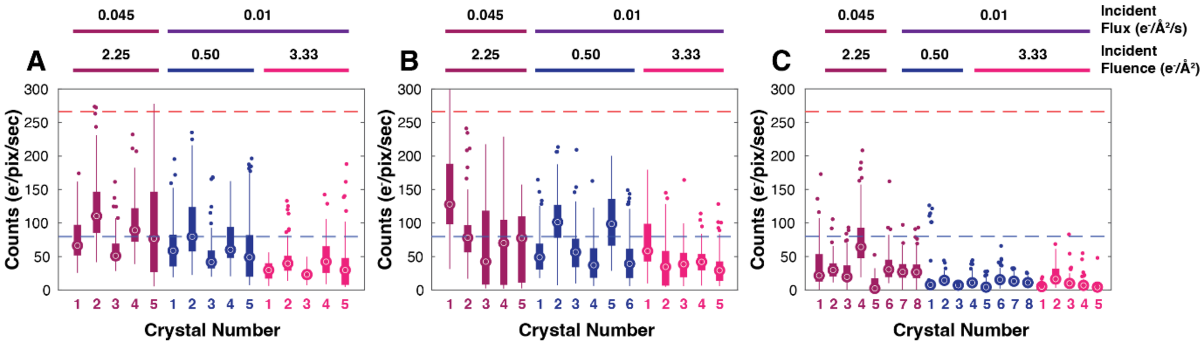

Figure 2 Analysis of measured counts in EBEC MicroED datasets with different incident beam fluence. Crystals were exposed to three different levels of total incident beam fluence: 0.5 (blue), 2.25 (magenta), and 3.33 (pink) $e^{-}/Å^{2}/s$. Box plots show the distribution of counts in measured reflections for each crystal of salen ligand (A), biotin (B), and thiostrepton (C). For each crystal, an open circle shows the median, boxes show the bounds of the upper and lower quartiles, and dots mark outliers. A dashed blue line marks 80 e^{-}/pix/s, while a red dashed line marks 266 e^{-}/pix/s.

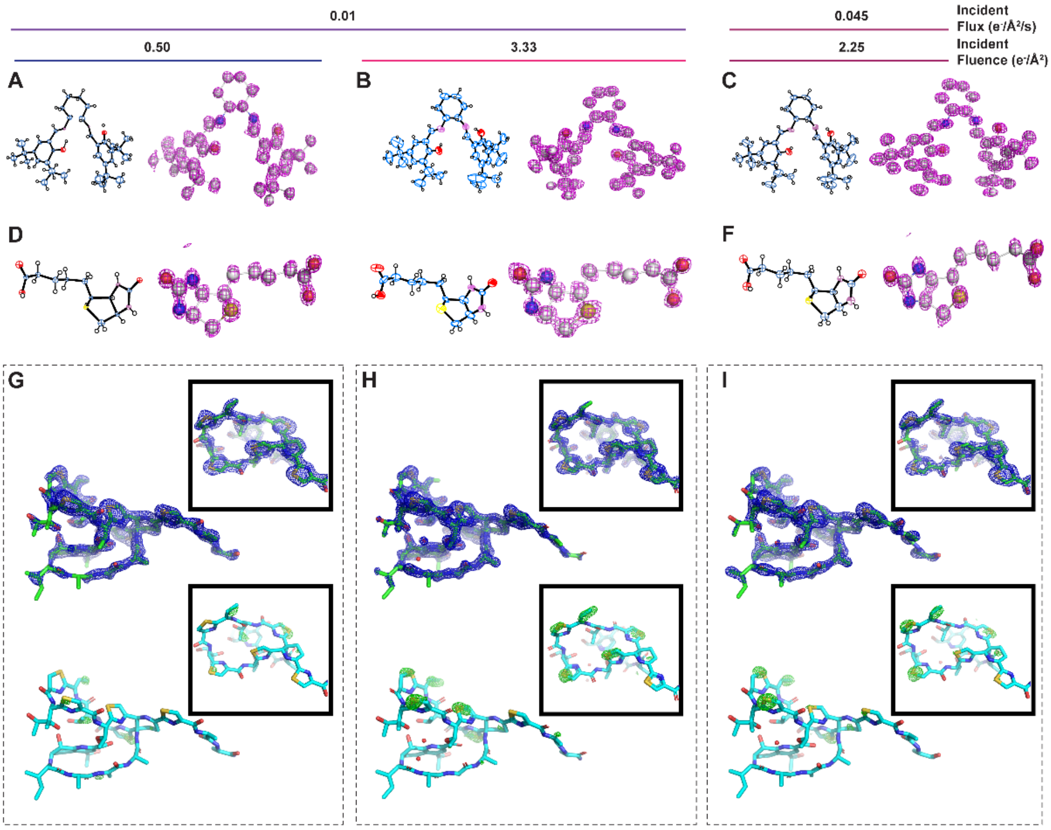

Figure 3 Structures of salen ligand (A-C), biotin (D-F), and thiostrepton (G-I) determined from EBEC MicroED data collected with different incident electron beam fluxes. For both salen ligand and biotin molecules, ORTEP diagrams and 3D models with F_o density map contoured at 2σ. Single crystals were exposed to a total fluence of 0.5 e$^-$/Å^2 (2 °/s rotation, 2 integrated frames/s, 0.01 e$^-$/Å^2/s flux density, panels A, D, G), 3.33 e$^-$/Å^2 (0.3 °/s rotation, 0.3 integrated frames/s, 0.01 e$^-$/Å^2/s flux density, panels B, E, H), and 2.25 e$^-$/Å^2 (2 °/s rotation, 2 integrated frames/s, 0.045 e$^-$/Å^2/s flux density, panels C, F, I). Hydrogen atoms were included in refinement and are displayed in ORTEP diagrams, but were excluded from ball and stick models for clarity. Structures of thiostrepton are drawn as green models with superimposed blue $2F_o$-F_c maps contoured at 1.8σ. Each is determined from a single crystal to 2.0 Å resolution (G), 1.5 Å resolution (H), and 1.8 Å resolution (I). Beneath each is the same model (cyan) superimposed with a green F_o-F_c map at 3σ, calculated from rigid body refinement of the measured data against a poly-alanine model of thiostrepton.

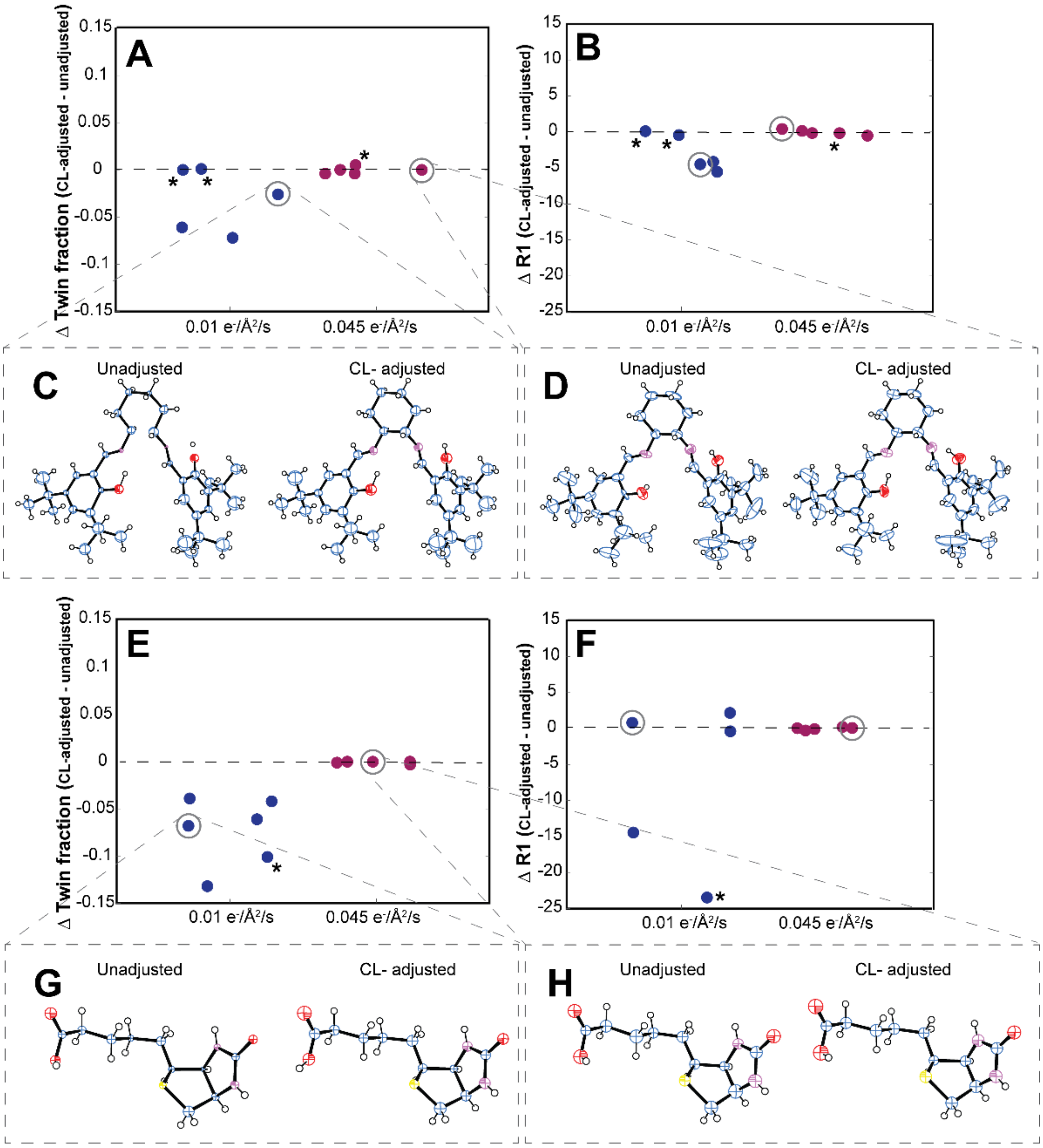

Figure 4 Analysis of CL-adjusted EBEC data. Change in estimated twin fraction (A, E) and achievable R1 (B, F) from the refinement for fast EBEC datasets as a result of CL adjustment, from crystals of the salen ligand (A–D) and biotin (E–H). Points denote data acquired with an incident flux of 0.01 $e^{-}/Å^{2}/s$ (blue) and datasets acquired with an incident flux of 0.045 $e^{-}/Å^{2}/s$ (magenta). Small molecule structures determined from data with and without CL-adjustment are shown for representative points, outlined in gray for salen ligand (C, D) and biotin (G, H). Anisotropic refinement of ADPs was performed where it did not result in ADP refinement to non-positive-definite (NPD) values. Asterisks (F) denote datasets for which refinements were unstable and did not yield a suitable refined structure.

Supplemental Material for “**Fast event-based electron counting for small molecule structure determination by MicroED**”

Appendices, supplementary scripts and tables.

Supplementary script 1. Calculation of CL estimates for a given incident electron flux per pixel per second. This script requires an explicit count rate and conversion of counts to electrons. It is configured to run in Matlab version 2023b, in a parallelized manner, with access to 16 cores.

```
function[countsout,lostcounts]=ebecsim()
%Required:
%anticipated detector count rate (per pix per sec)
%flux range (per pix per sec)
%ntrials = number of measurements simulated

%% COUNTING SIMULATION

countrate=2392; %internal detector count rate (e-/pix/s)
fluxin=500; %incident beam flux (e-/pix/s)
cpix=9; %number of correlated pixels used during counting and centroiding
ntrials=1000; %number of independent measurements simulated

countsout = ones(fluxin,ntrials,'single');
lostcounts = zeros(fluxin,ntrials,'single');

for aa=2:fluxin
    for bb=1:ntrials
        rng("shuffle");
        diste=randi([1 countrate],1,cpix.*aa);
        grosscounts=hist(diste,1:countrate);
        netcounts=grosscounts;
        netcounts(netcounts>0)=1;
        ncounts=sum(netcounts)./cpix;
        countsout(aa,bb)=ncounts;
        lcounts=(sum(grosscounts)./cpix)-ncounts;
        lostcounts(aa,bb)=lcounts;
    end
end
```

Supplementary script 2. SerialEM script for EBEC data collection of continuous rotation MicroED data on the Apollo detector. The script assumes crystal locations have been saved in the navigator and recalls those locations for a set number of items. It also allows for multiple sweeps to be recorded from a single crystal. Lastly, the script assumes the Apollo detector is inserted and gain normalized, and that it is configured, within the SerialEM environment to record exposures of the desired time/degree length.

```
ScriptName BatchED

SetColumnOrGunValve 1
SetBeamBlank 0

nitems = 5
xtalct = 1
Startangle = 50
Finalangle = -50
nsweeps = 1
rotrate = 0.0666

Loop $nitems
   xtalct = $xtalct + 1
   sweepcount = 1
   SetFolderForFrames mov$xtalct_sweep$sweepcount
   MoveToNavItem $xtalct

   Loop $nsweeps
      sweepcount = $sweepcount + 1
      TiltTo $Startangle
      Delay 2 sec
      GoToLowDoseArea S
      UseContinuousFrames 1

      echo STARTING TILT
      BackgroundTilt $Finalangle $rotrate
      Delay 1 sec
      ReportStageXYZ
      Search
      StopContinuous

      echo END TILT
      ReportClock
      ReportStageXYZ
      Delay 20 sec
   EndLoop

EndLoop
```

Supplementary script 3. Adjustment of electron counts per pixel per second in a given dataset, to account for anticipated CL as calculated in Supplementary script 1. The raw, super-resolution MRC file written by the Apollo, the pre-calculated simulations of CL generated by Supplementary Script 1, and an output name are required as inputs to this script, The CL-adjustment script is configured to run in Matlab version 2023b; the code can be executed in parallel, with access to sufficient memory resources.

```
function[diffstackout,cl_residuals]=mrc_clfix(diffstackin,ebecsimdata)
% Required:
%diffstackin: diffraction data matrix
%ebecsimdata: data file containing simulated CL for a given detector

cmin=10;
cmax=266;
ctstoelectrons=16;
fps=2;

load(ebecsimdata,'countsout','lostcounts');
ctsmean=mean(countsout,2);
clmean=mean(lostcounts,2);

diffstackout=diffstackin;
for jj=cmin:cmax
    tmpstack=abs(diffstackin-jj);
    tmpstack(tmpstack>2)=0;
    tmpstack(tmpstack>0)=1;
    pixpool=sum(sum(sum(tmpstack)));
    if pixpool>1
        [~,fluxin]=min(abs(ctsmean-jj));
        closs=clmean(fluxin);
        diffstackout(tmpstack==1)=diffstackout(tmpstack==1) + closs;
    end
end

cl_residuals=diffstackout-diffstackin;
```

Supplementary Table 1 Electron counts as a function of incident beam flux in static MicroED data collected from salen ligand crystals on the Apollo detector.

Condition	**Maximum Counts (e^-/pix/s)**			**Maximum percentage of signal pixels with counts > 80 e^-/pix/s per frame**		
Spot size	9	10	11	9	10	11
Incident flux (e^-/Å^2/s)	0.045	0.03	0.01	0.045	0.03	0.01
Crystal 1	203	196	246	5.3	5.2	4.5
Crystal 2	114	103	49	3.1	2.8	1.7
Crystal 3	107	13	8	2.1	1.6	1.2
Crystal 4	-	107	87	-	2.4	1.9
Crystal 5	131	91	53	3.2	2.7	2.6
Crystal 6	71	60	26	3.3	2.5	2.9

Supplementary Table 2 Difference map peaks greater than 3σ in EBEC structures of thiostrepton determined at different incident fluence, when the data is refined against a model of thiostrepton mutated to poly-alanine

Total incident fluence ($e^-/Å^2$)	Residue/sidechain/heteroatom	Sigma level of peak
0.50	Residue 6 thiazole	+4.04 RMSD
	Water	+3.72 RMSD
	Residue 7 threonine sidechain	+3.48 RMSD
	Residue 11 thiazole	+3.40 RMSD
	Residue 3 ethylene	+3.34 RMSD
3.33	Residue 11 thiazole	+5.81 RMSD
	Residue 13 thiazole	+5.04 RMSD
	Residue 6 thiazole	+4.60 RMSD
	Residue 8 dehydrobutyrine sidechain	+4.08 RMSD
	Residue 9 thiazole	+3.90 RMSD
	Residue 16 ethylene	+3.32 RMSD
	Residue 12 threonine sidechain	+3.14 RMSD
	Residue 15 thiazole	+3.02 RMSD
2.25	Residue 11 thiazole	+5.70 RMSD
	Residue 8 dehydrobutyrine sidechain	+4.37 RMSD
	Residue 6 thiazole	+4.28 RMSD
	Residue 9 thiazole	+4.10 RMSD
	Residue 15 thiazole	+3.39 RMSD
	Residue 13 thiazole	+3.31 RMSD
	Water	+3.01 RMSD

Supplementary Table 3 Twin law test results (Reported as <L> ; <L^2> ; **Estimated twin fraction**) of unmodified and CL-adjusted EBEC MicroED datasets.

Spot size	9	9	11	11	11	11
Flux (e$^-$ / Å^2 /s)	0.045	0.045	0.01	0.01	0.01	0.01
Rotation rate (deg/s)	2	2	2	2	0.3	0.3
CL-adjusted	-	+	-	+	-	+
Salen ligand						
Crystal 1	0.490; 0.321; **0**	0.490; 0.313; **0.011**	0.433; 0.261; **0.119**	0.466; 0.294; **0.047**	0.505; 0.339; **0**	0.477; 0.308; **0.030**
Crystal 2	0.481; 0.321; **0.011**	0.483; 0.313; **0.020**	0.460; 0.287; **0.057**	0.476; 0.305; **0.031**	0.496; 0.329; **0**	0.480; 0.311; **0.025**
Crystal 3	0.482; 0.310; **0.024**	0.483; 0.313; **0.021**	0.441; 0.267; **0.097**	0.473; 0.301; **0.036**	0.507; 0.340; **0**	0.463; 0.292; **0.052**
Crystal 4	0.489; 0.318; **0.013**	0.492; 0.321; **0.009**	0.493; 0.323; **0.007**	0.493; 0.324; **0.007**	0.515; 0.350; **0**	0.502; 0.335; **0**
Crystal 5	0.482; 0.313; **0.023**	0.477; 0.307; **0.028**	0.481; 0.314; **0.023**	0.480; 0.311; **0.024**	0.519; 0.357; **0**	0.510; 0.347; **0**
Biotin						
Crystal 1	0.516; 0.350; **0**	0.518; 0.352; **0**	0.439; 0.266; **0.102**	0.474; 0.301; **0.034**	0.510; 0.342; **0**	0.466; 0.294; **0.047**
Crystal 2	0.495; 0.325; **0.006**	0.495; 0.325; **0.005**	0.448; 0.273; **0.083**	0.482; 0.311; **0.022**	0.547; 0.386; **0**	0.501; 0.334; **0**
Crystal 3	0.525; 0.359; **0**	0.533; 0.368; **0**	0.432; 0.258; **0.121**	0.448; 0.274; **0.082**	0.528; 0.364; **0**	0.502; 0.333; **0**
Crystal 4	0.477; 0.304; **0.029**	0.479; 0.305; **0.026**	0.428; 0.260; **0.132**	0.498; 0.330; **0**	0.506; 0.335; **0**	0.466; 0.294; **0.046**
Crystal 5	0.500; 0.331; **0**	0.498; 0.329; **0**	0.469; 0.296; **0.042**	0.505; 0.335; **0**	0.511; 0.344; **0**	0.490; 0.320; **0.012**
Crystal 6	N/A	N/A	0.440; 0.269; **0.101**	0.496; 0.327; **0**	N/A	N/A
Thiostrepton						
Crystal 1	0.450; 0.278; **0.077**	N/A	0.466; 0.297; **0.048**	N/A	0.419; 0.247; **0.159**	N/A

Crystal 2	0.463; 0.293; **0.052**	N/A	0.445; 0.273; **0.081**	N/A	0.469; 0.299; **0.042**	N/A
Crystal 3	0.447; 0.277; **0.083**	N/A	0.454; 0.283; **0.069**	N/A	0.465; 0.295; **0.048**	N/A
Crystal 4	0.463; 0.293; **0.053**	N/A	0.481; 0.315; **0.023**	N/A	0.478; 0.307; **0.028**	N/A
Crystal 5	0.458; 0.288; **0.061**	N/A	N/A	N/A	N/A	N/A
Crystal 6	0.474; 0.303; **0.034**	N/A	N/A	N/A	N/A	N/A

Supplementary Table 4 Crystallographic data reduction statistics for MicroED datasets from individual crystals of the salen ligand collected first on the Ceta-D detector, and then on the Apollo detector, with an incident flux of 0.01 e^-/Å^2/s, and equivalent rotation and sampling rates.

Crystal	**1**	**1**	**2**	**2**
Electron Flux (e^- / Å^2 /s)	0.01	0.01	0.01	0.01
Total Fluence (e^- / Å^2)	0.5	0.5	0.5	0.5
Stage rotation rate (°/s)	2	2	2	2
Data collection time (s)	50	50	50	50
Detector	Apollo	Ceta-D	Apollo	Ceta-D
Frame rate (Hz)	2	2	2	2
Data Processing				
Resolution (Å)	20 – 0.8 (0.9-0.8)	20 – 0.8 (0.9-0.8)	20 – 0.8 (0.9-0.8)	20 – 0.8 (0.9-0.8)
# total reflections	13394 (3671)	13682 (3175)	13328 (3706)	13404 (3029)
# unique reflections	3469 (989)	3539 (842)	2670 (777)	2670 (622)
R$_{merge}$ (%)	22.10 (38.20)	54.20 (1344.20)	25.40 (90.00)	63.80 (9624.80)
CC1/2 (%)	97.8 (36.8)	94.0 (-7.5)	97.7 (24.3)	93.2 (-4.2)
<I/σI>	4.35 (3.36)	1.42 (0.09)	4.05 (1.53)	1.62 (0.00)
Completeness (%)	92.40 (91.90)	88.20 (72.80)	71.60 (72.30)	66.70 (53.90)
Crystal	**3**	**3**	**4**	**4**
Electron Flux (e^- / Å^2 /s)	0.01	0.01	0.01	0.01
Total Fluence (e^- / Å^2)	0.5	0.5	0.5	0.5
Stage rotation rate (°/s)	2	2	2	2
Data collection time (s)	50	50	50	50
Detector	Apollo	Ceta-D	Apollo	Ceta-D
Frame rate (Hz)	2	2	2	2
Data Processing				
Resolution (Å)	20 – 0.8 (0.9-0.8)	20 – 0.8 (0.9-0.8)	20 – 0.8 (0.9-0.8)	20 – 0.8 (0.9-0.8)
# total reflections	13408 (3780)	13639 (3058)	13351 (3675)	12507 (3215)
# unique reflections	3676 (1057)	3651 (830)	2065 (606)	2068 (538)
R$_{merge}$ (%)	21.00 (83.90)	55.90 (980.40)	16.30 (21.60)	48.00 (716.70)
CC1/2 (%)	98.3 (33.6)	95.6 (2.4)	98.9 (59.3)	97.5 (-12.9)
<I/σI>	3.85 (1.20)	1.59 (0.10)	7.40 (6.54)	1.77 (1.77)
Completeness (%)	98.30 (98.90)	90.40 (71.70)	55.70 (57.0)	51.80 (46.90)
Crystal	**5**	**5**		

Electron Flux (e$^-$ / Å^2 /s)	0.01	0.01
Total Fluence (e$^-$ / Å^2)	0.5	0.5
Stage rotation rate (°/s)	2	2
Data collection time (s)	50	50
Detector	Apollo	Ceta-D
Frame rate (Hz)	2	2
Data Processing		
Resolution (Å)	20 – 0.8 (0.9-0.8)	20 – 0.8 (0.9-0.8)
# total reflections	12426 (3752)	14397 (3846)
# unique reflections	3633 (1046)	3825 (1006)
R$_{merge}$ (%)	22.10 (78.60)	56.30 (-99.90)
CC1/2 (%)	97.7 (19.7)	93.9 (-14.0)
<I/σI>	3.75 (1.47)	1.43 (0.00)
Completeness (%)	97.40 (97.80)	94.90 (86.50)

Supplementary Table 5 Crystallographic data reduction statistics for MicroED datasets from individual crystals of the salen ligand collected first on the Ceta-D detector, and then on the Apollo detector, with an incident flux of 0.045 e^-/Å^2/s, and equivalent rotation and sampling rates.

Crystal	**1**	**1**	**2**	**2**
Electron Flux (e^- / Å^2 /s)	0.045	0.045	0.045	0.045
Total Fluence (e^- / Å^2)	2.25	2.25	2.25	2.25
Stage rotation rate (°/s)	2	2	2	2
Data collection time (s)	50	50	50	50
Detector	Apollo	Ceta-D	Apollo	Ceta-D
Frame rate (Hz)	2	2	2	2
Data Processing				
Resolution (Å)	20 – 0.8 (0.9-0.8)	20 – 0.8 (0.9-0.8)	20 – 0.8 (0.9-0.8)	20 – 0.8 (0.9-0.8)
# total reflections	9800 (2693)	14261 (3959)	12898 (3530)	14057 (3628)
# unique reflections	2556 (728)	2703 (750)	3409 (950)	3505 (888)
R_{merge} (%)	19.00 (253.30)	30.50 (896.90)	20.10 (77.70)	64.90 (-99.90)
CC1/2 (%)	98.7 (2.8)	98.5 (-3.5)	98.3 (31.8)	93.7 (-5.5)
<I/σI>	3.23 (0.48)	3.14 (0.18)	4.3 (1.52)	1.33 (0.00)
Completeness (%)	68.30 (67.50)	67.50 (65.30)	90.70 (88.70)	86.40 (75.60)
Crystal	**3**	**3**	**4**	**4**
Electron Flux (e^- / Å^2 /s)	0.045	0.045	0.045	0.045
Total Fluence (e^- / Å^2)	2.25	2.25	2.25	2.25
Stage rotation rate (°/s)	2	2	2	2
Data collection time (s)	50	50	50	50
Detector	Apollo	Ceta-D	Apollo	Ceta-D
Frame rate (Hz)	2	2	2	2
Data Processing				
Resolution (Å)	20 – 0.8 (0.9-0.8)	20 – 0.8 (0.9-0.8)	20 – 0.8 (0.9-0.8)	20 – 0.8 (0.9-0.8)
# total reflections	13161 (3655)	14458 (4048)	13210 (3665)	14410 (4037)
# unique reflections	2572 (730)	2830 (802)	2262 (650)	2358 (669)
R_{merge} (%)	13.80 (99.80)	21.10 (227.20)	15.30 (100.50)	20.50 (216.70)
CC1/2 (%)	99.3 (29.6)	98.9 (2.5)	99.0 (46.4)	98.5 (23.0)
<I/σI>	5.99 (1.35)	3.9 (0.57)	5.92 (1.39)	4.44 (0.72)
Completeness (%)	68.60 (67.80)	70.80 (69.90)	60.40 (60.40)	58.90 (58.30)
Crystal	**5**	**5**		

Electron Flux (e$^-$ / Å^2 /s)	0.045	0.045
Total Fluence (e$^-$ / Å^2)	2.25	2.25
Stage rotation rate (°/s)	2	2
Data collection time (s)	50	50
Detector	Apollo	Ceta-D
Frame rate (Hz)	2	2
Data Processing		
Resolution (Å)	20 – 0.8 (0.9-0.8)	20 – 0.8 (0.9-0.8)
# total reflections	13352 (3699)	14566 (4085)
# unique reflections	2719 (773)	2886 (827)
R_{merge} (%)	22.40 (378.00)	26.20 (307.20)
CC1/2 (%)	99.1 (0.3)	97.9 (9.1)
<I/σI>	3.63 (0.37)	3.20 (0.44)
Completeness (%)	72.60 (71.80)	71.90 (71.70)

Supplementary Table 6 List of Zenodo archive entries where diffraction data from this report is accessible.

Dataset	**Zenodo DOI**
EBEC diffraction tilt series on biotin nanocrystals at variable total fluence	https://zenodo.org/doi/10.5281/zenodo.13690162
EBEC diffraction tilt series on salen ligand nanocrystals at variable total fluence	https://zenodo.org/doi/10.5281/zenodo.13713098
EBEC diffraction tilt series on thiostrepton nanocrystals at variable total fluence	https://zenodo.org/doi/10.5281/zenodo.13716076
EBEC diffraction movies over a range of incident flux on salen ligand crystals	https://zenodo.org/doi/10.5281/zenodo.13716389
EBEC diffraction movies over a range of incident flux on salen ligand crystals	https://zenodo.org/doi/10.5281/zenodo.13716389
Diffraction tilt series recorded on the DE Apollo and Ceta D camera for the same salen ligand crystals, at variable incident flux	https://zenodo.org/doi/10.5281/zenodo.13716389

Supplementary figures.

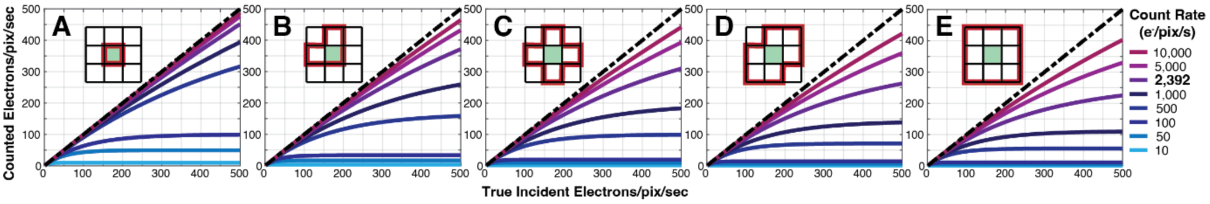

Supplementary figure 1. Simulated electron counts from different clusters of pixels, sampled on a one second interval with a given count rate. Sampled count rates: 10, 50, 100, 500, 1000, 2392, 5000 and 10000 e^-/pix/s. Curves show the effect of the varied internal pixel count rates on the expected total count of electrons per pixel for a given true electron flux on that pixel assuming no correlation with its neighbors (A), and a progressively larger cluster of pixels considered during counting: 3, 5, 7, and 9 (B-E). A dashed black line denotes the hypothetical line corresponding to perfect counting. The maximum internal count rate for the Apollo detector is denoted in bold: 2,392 e^-/pix/s.

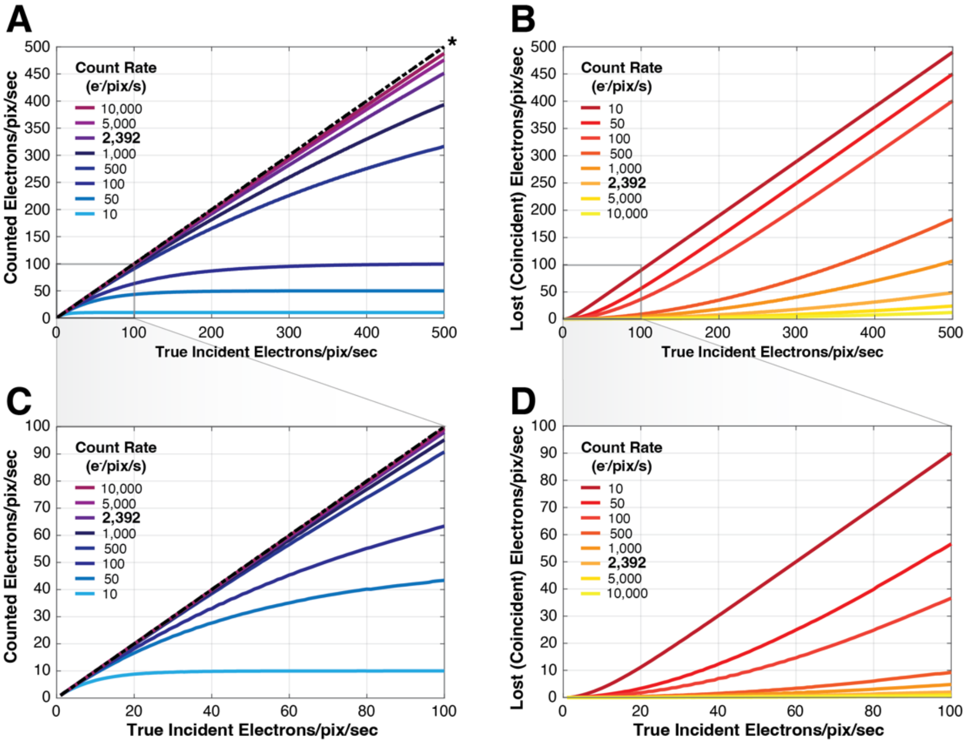

Supplementary figure 2. Simulated electron counts from a single hypothetical pixel, sampled on a one second interval with a given count rate. Sampled count rates: 10, 50, 100, 500, 1000, 2392, 5000 and 10000 e^-/pix/s. Curves show the effect of the varied internal pixel count rates on the expected total count of electrons per pixel for a given true electron flux on that pixel (A). For each count rate, the expected count of electrons lost due to coincidence is shown as a function of incident electron flux on a pixel (B). Insets (C,D) magnify the region from 0 to 100 e^-/pix/s in (A,B). A star (A) denotes the hypothetical line corresponding to perfect counting. The maximum internal count rate for the Apollo detector is denoted in bold: 2,392 e^-/pix/s.

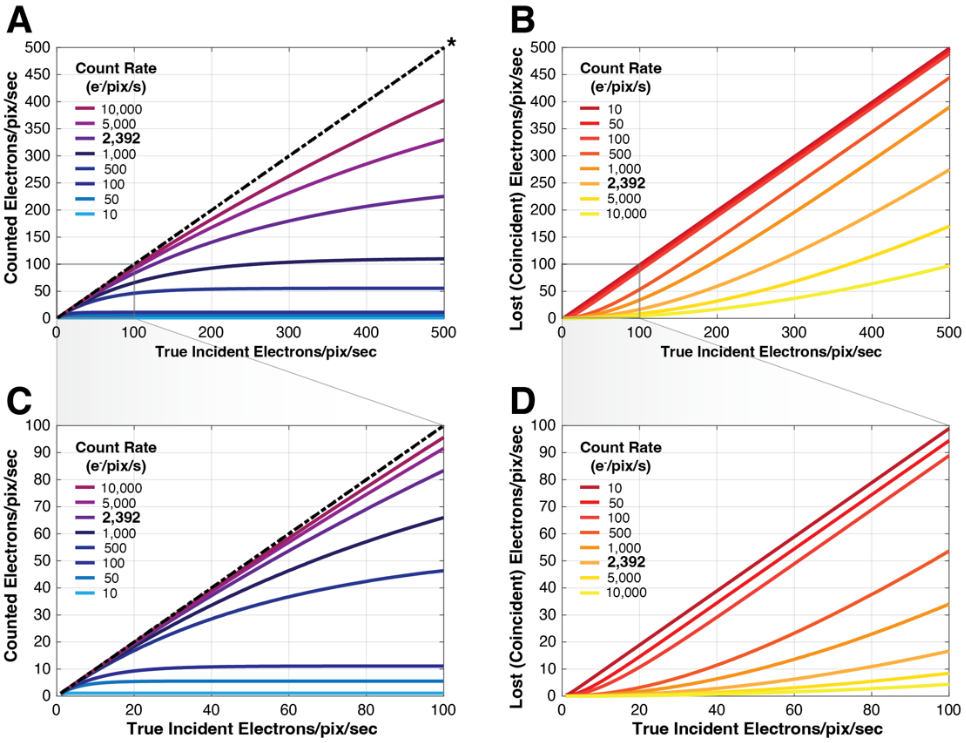

Supplementary figure 3. Simulated electron counts from a 3x3 cluster of hypothetical pixels, sampled on a one second interval with a given count rate per pixel. Sampled count rates: 10, 50, 100, 500, 1000, 2392, 5000 and 10000 e$^-$/pix/s. Curves show the effect of the varied internal pixel count rates on the expected total count of electrons per pixel for a given true electron flux on that pixel (A). For each count rate, the expected count of electrons lost due to coincidence is shown as a function of incident electron flux on a pixel (B). Insets (C,D) magnify the region from 0 to 100 e$^-$/pix/s in (A,B). A star (A) denotes the hypothetical line corresponding to perfect counting. The maximum internal count rate for the Apollo detector is denoted in bold: 2,392 e$^-$/pix/s.

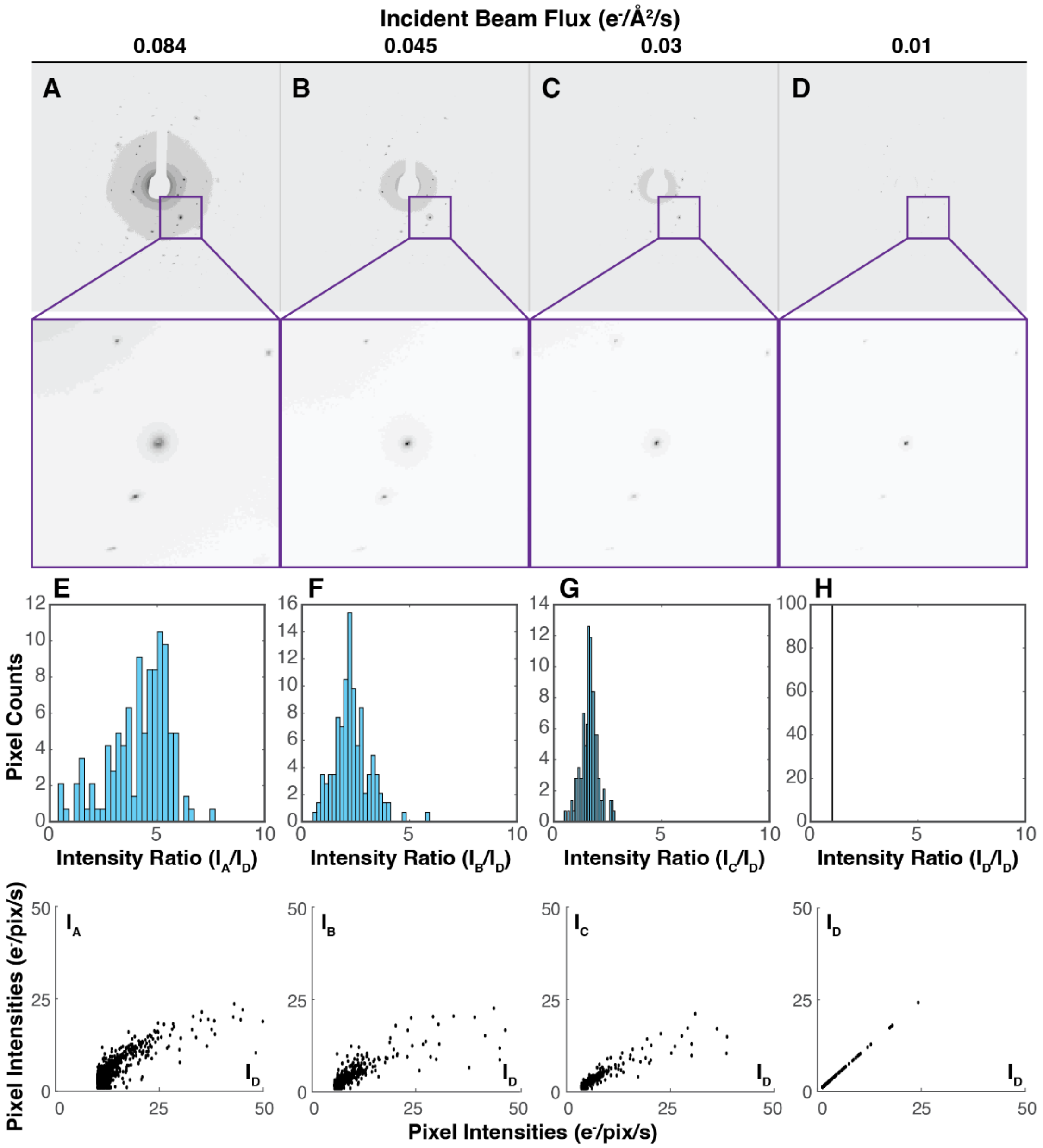

Supplementary figure 4. Measured diffraction from well ordered, highly diffracting nanocrystals of Co(II) meso-tetraphenyl porphyrin. (A-D) Diffraction obtained from the same illuminated region of the same crystal at increasing incident flux values, from 0.01 to 0.084 e$^-$/Å^2/s. Insets show a magnified view of reflections observed in outlined purple boxes, highlighting the strongest incident reflection. (E-H) Histograms of ratios of electrons counted in diffraction patterns shown in panels A-C, vs. panel D (top). All count ratios in panel H are 1, since values there are comparing panel D counts to themselves; all other count ratios are greater than zero. While most counts are greater than one in panels A-C, some counts are less than one, indicating loss of counts in higher incident flux patterns due to coincidence, or other count restrictions. Scatterplots (bottom) for each of E-H, compare electron counts for individual pixels in conditions A-C to those in D. Only pixels with values greater than 1 were considered in the analysis. Electron counts along the horizontal axis are for flux values in D, scaled by the corresponding flux values in A-C.

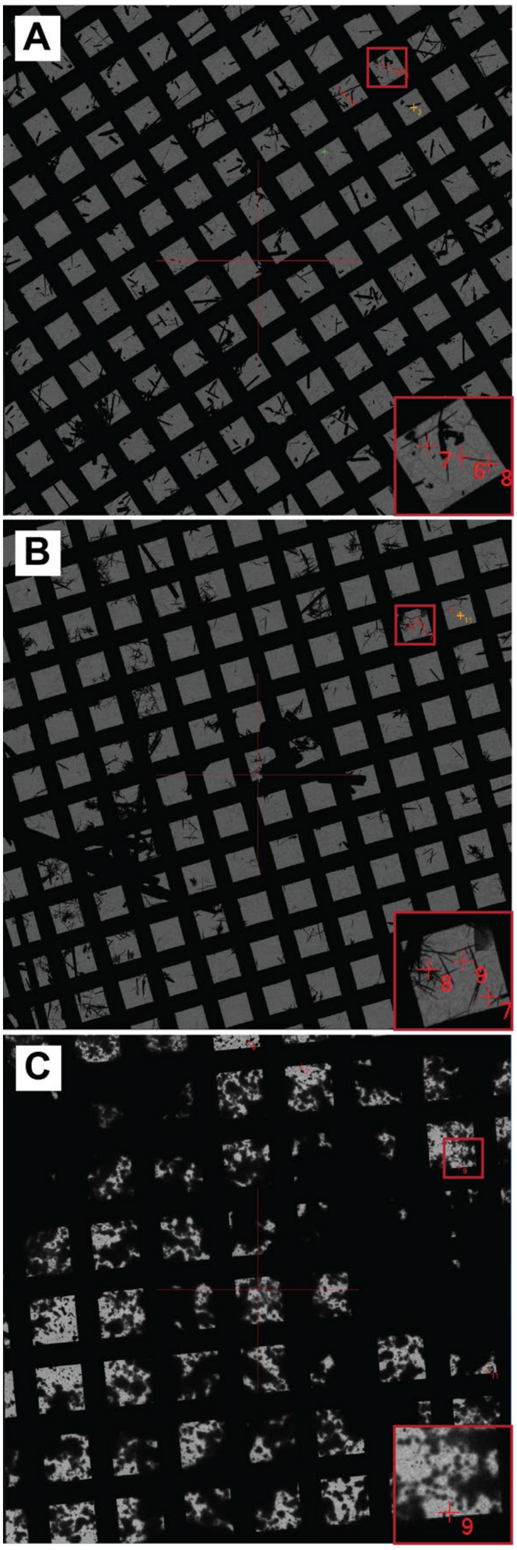

Supplementary figure 5. Overviews of grids containing salen ligand (A), biotin (B), and thiostrepton (C) crystals. Each overview is a montage of images pieced together by serialEM, and each is used to select crystals for fast EBEC MicroED data collection in automated fashion using serialEM. For each panel, red boxes outline a region of the grid that was targeted for data collection, and insets show the numbered locations of targeted crystals.

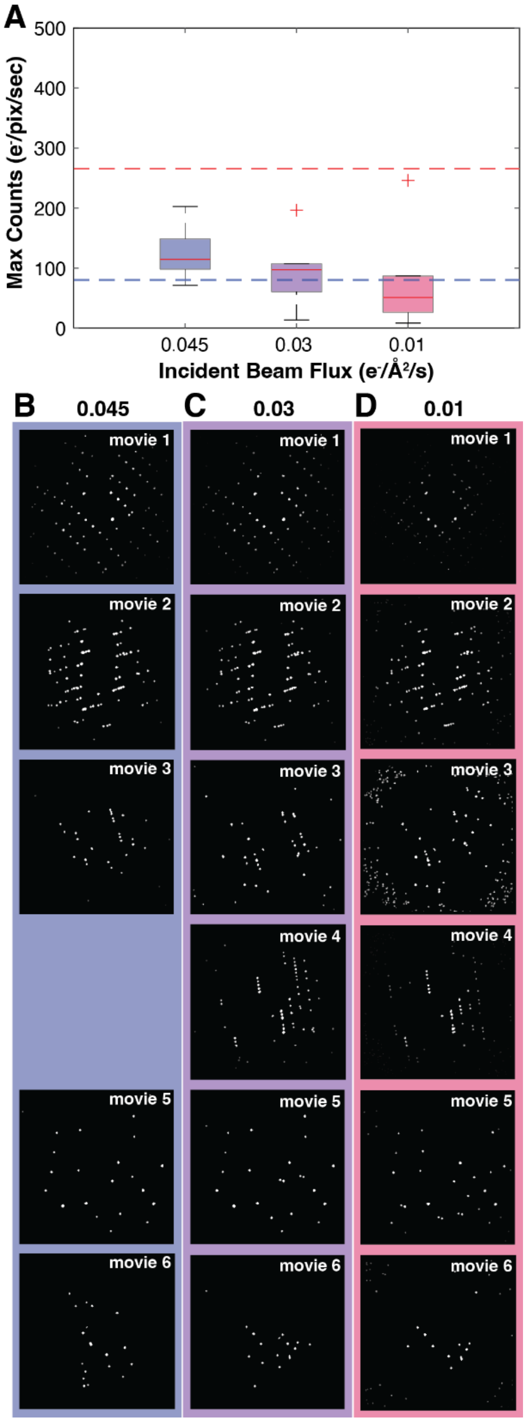

Supplementary figure 6. Analysis of diffraction recorded from salen ligand crystals illuminated with different incident beam flux. (A) The distribution of maximum counts recorded per pixel over a given dataset is shown for three incident beam flux conditions, 0.01, 0.03 and 0.045 $e^-/Å^2/s$; the dashed red line indicates 266 e^-/pix/s and dashed blue line, 80 e^-/pix/s. Each box charts the mean of and first and fourth quartiles of a maximum counts distribution; red crosses denote outliers. Maximum projections of all reflections detected in each dataset recorded for the different incident beam flux conditions are shown in (B-D). For numbered movie the same crystal was diffracted at the different incident beam flux values, yielding three congruent sets of patterns of varying diffraction intensity; movie 4 at the highest incident flux could not be processed due to a technical malfunction.

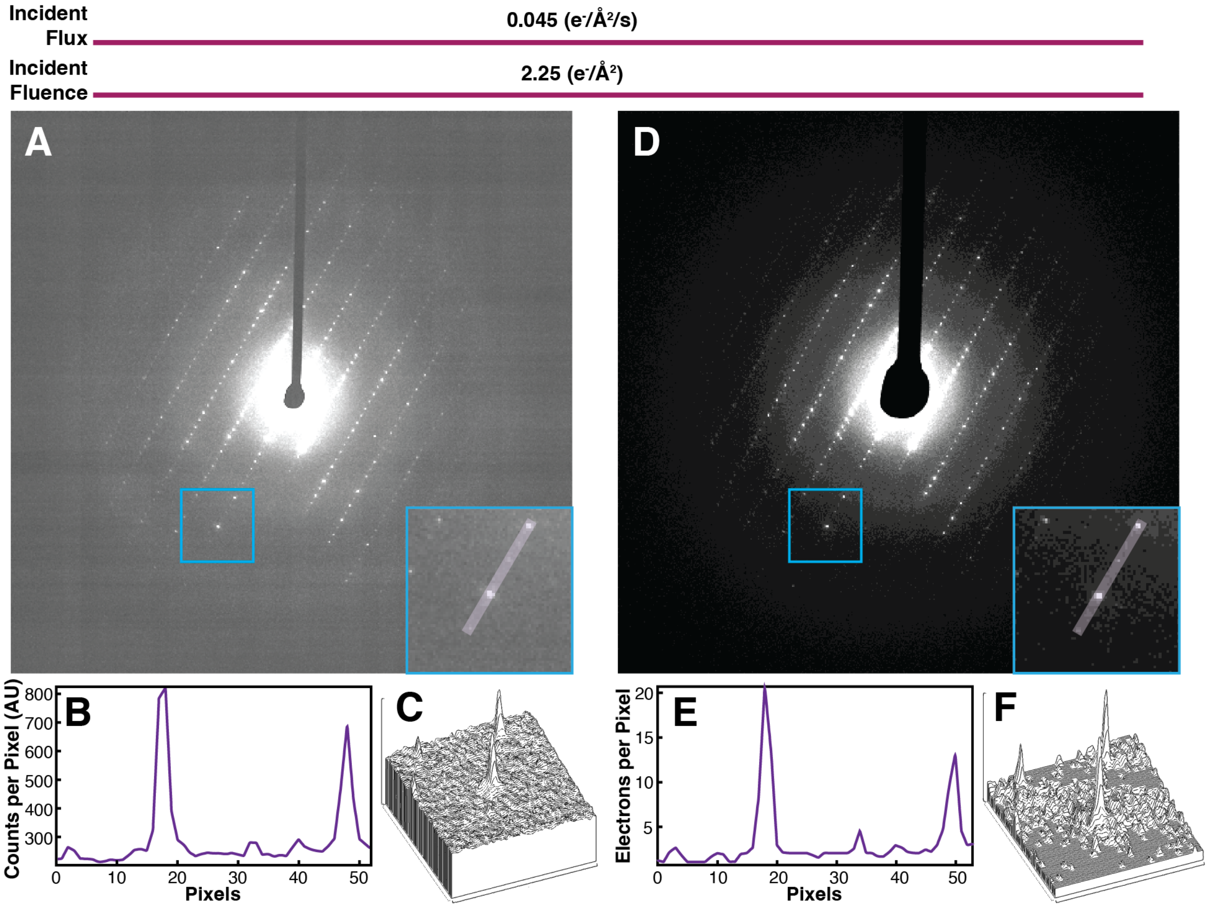

Supplementary figure 7. EBEC MicroED data collected from salen ligand crystals illuminated with an incident beam flux of 0.045 $e^-/Å^2/s$. Data from the same crystal was collected under identical conditions using a CETA-D (A) or Apollo (D) detector. Each pattern shows a maximum projection of measured counts over the same 2 degrees of each dataset. Insets show a region of the pattern containing visible reflections. An intensity profile (B,E) is calculated for the transparent line traversing the reflections in each inset. A 3D profile of each inset is also shown (C,F). The intensity range sampled in (A) ranges from 0 to 500 counts, while in (B) it ranges from 0 to 10 e^-.

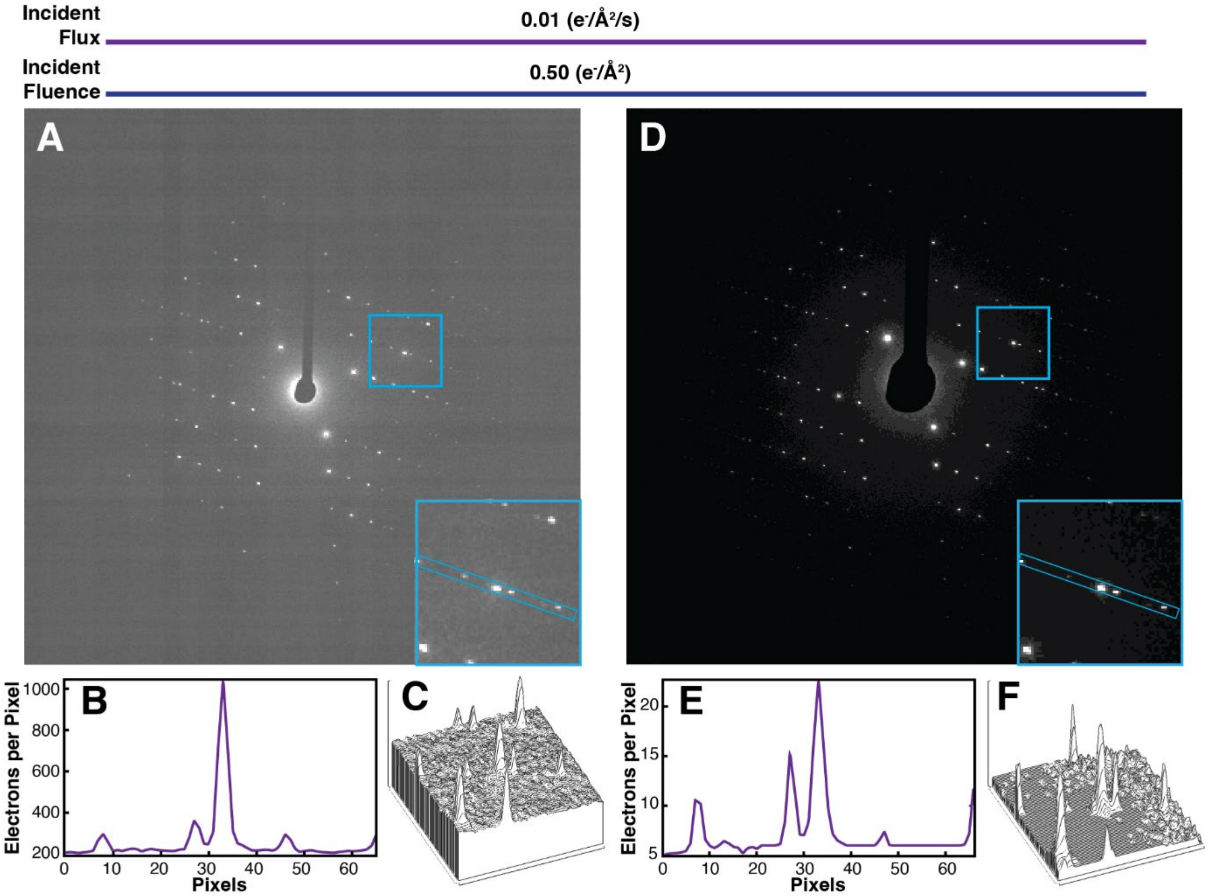

Supplementary figure 8. EBEC MicroED data collected from salen ligand crystals illuminated with an incident beam flux of 0.01 e$^-$/Å^2/s. Data from the same crystal was collected under identical conditions using a CETA-D (A) or Apollo (D) detector. Each pattern shows a maximum projection of measured counts over the same 2 degrees of each dataset. Insets show a region of the pattern containing visible reflections. An intensity profile (B,E) is calculated for the transparent line traversing the reflections in each inset. A 3D profile of each inset is also shown (C,F). The intensity range sampled in (A) ranges from 0 to 500 counts, while in (B) it ranges from 0 to 10 e$^-$.

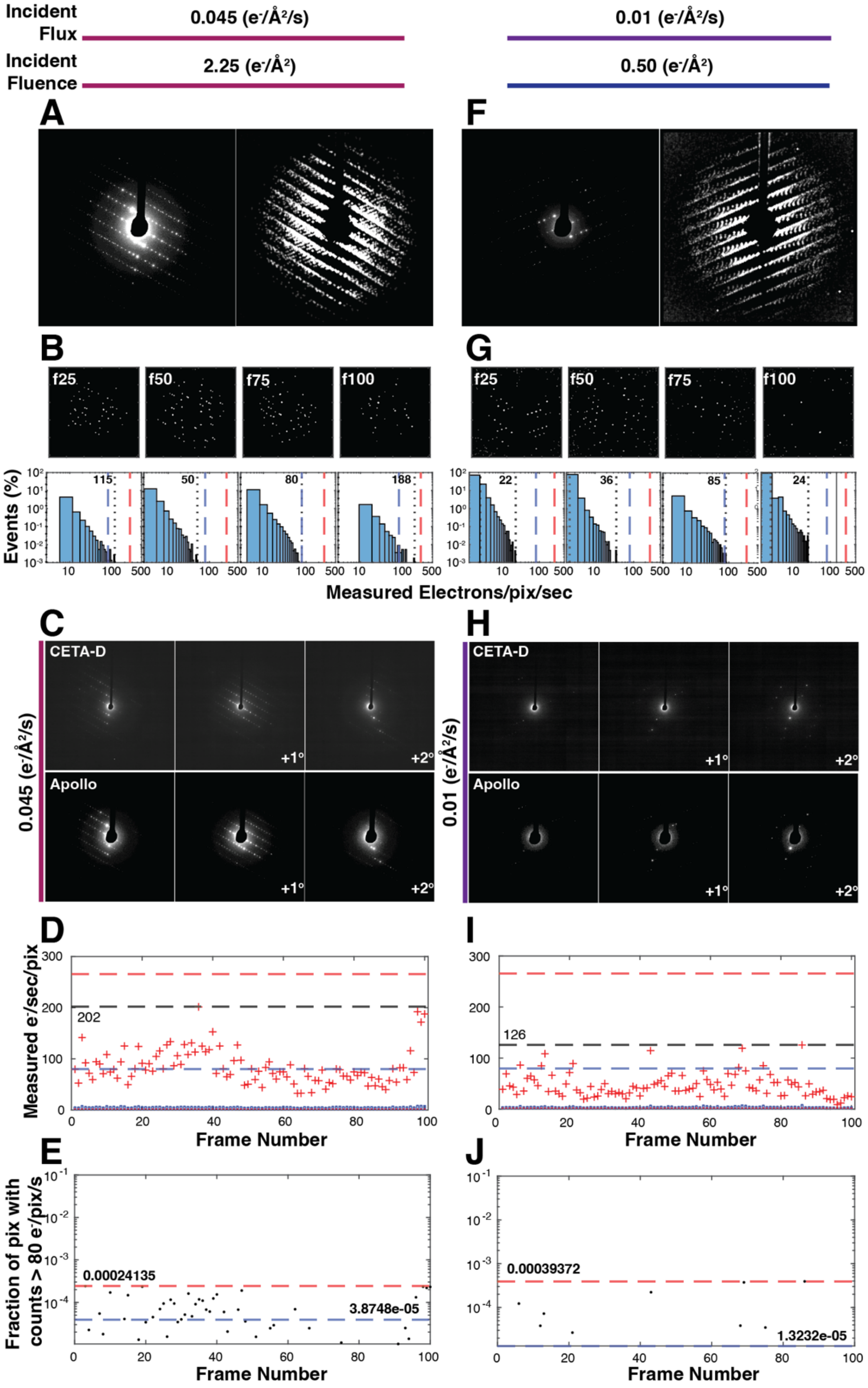

Supplementary figure 9. Comparison of diffraction patterns from salen ligand crystals illuminated by a high flux (A-E) or low flux (F-J) incident electron beam. Single patterns from a 100-frame MicroED dataset, spanning 100°, are shown alongside maximum projections of all identified reflections across the measured wedge of data (A,F). Sets of reflections identified in patterns 25, 50, 75 and 100 of each dataset are shown above the respective histograms of counts for each pattern (B,G). In each histogram, dashed blue lines mark 80 e^-/pix/s, dashed red lines 266 e^-/pix/s, and dashed black lines the maximum counts in that frame. A series of three diffraction frames, 1° apart, shows pairs of patterns collected under identical conditions on the Apollo or CETA-D detectors (C,H). The maximum counts in each of the 100 images in the pattern are shown as red crosses in plots of the distribution of measured pixels per frame (D, I). Here, again, dashed blue lines mark 80 e^-/pix/s, dashed red lines 266 e^-/pix/s, and dashed black lines the maximum counts across all frames. The fraction of pixels in each frame with counts above 80 e^-/pix/s are noted in (E,J), where a dashed blue line shows the mean fraction of such pixels across all frames, while the dashed red line shows the maximum fraction of such pixels across all frames.

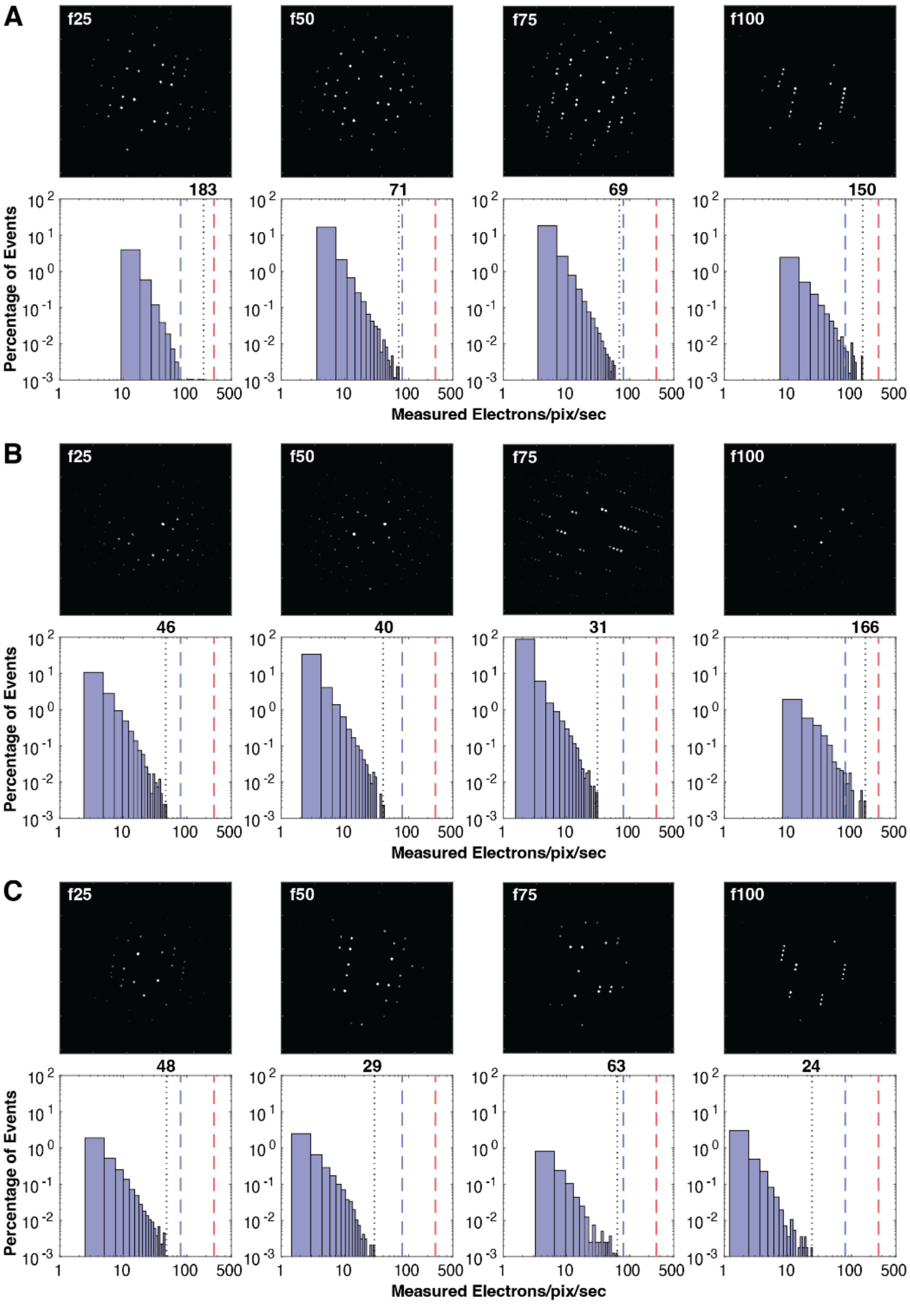

Supplementary figure 10. Representations of individual diffraction frames and histograms of electron count distributions for those frames, sampled from MicroED movies of salen ligand crystals. Reflections identified in each of four frames are shown; images correspond to frames 25, 50, 75 and 100 in a hundred-frame dataset. Three datasets sampled from three distinct salen ligand crystals are shown, with incident beam fluences of 2.25 (A) and 0.5 (B), and 3.33 (C) $e^{-}/Å^{2}/s$. On histogram plots, blue dashed lines denote 80 counted e^{-}/pix/s, red dashed lines indicate 266 e^{-}/pix/s, and black dashed lines indicate the maximum number of e^{-}/pix/s detected in the sampled frame. A dashed line and the number above it in histograms mark the maximum counts for each frame, in e^{-}/pix/s.

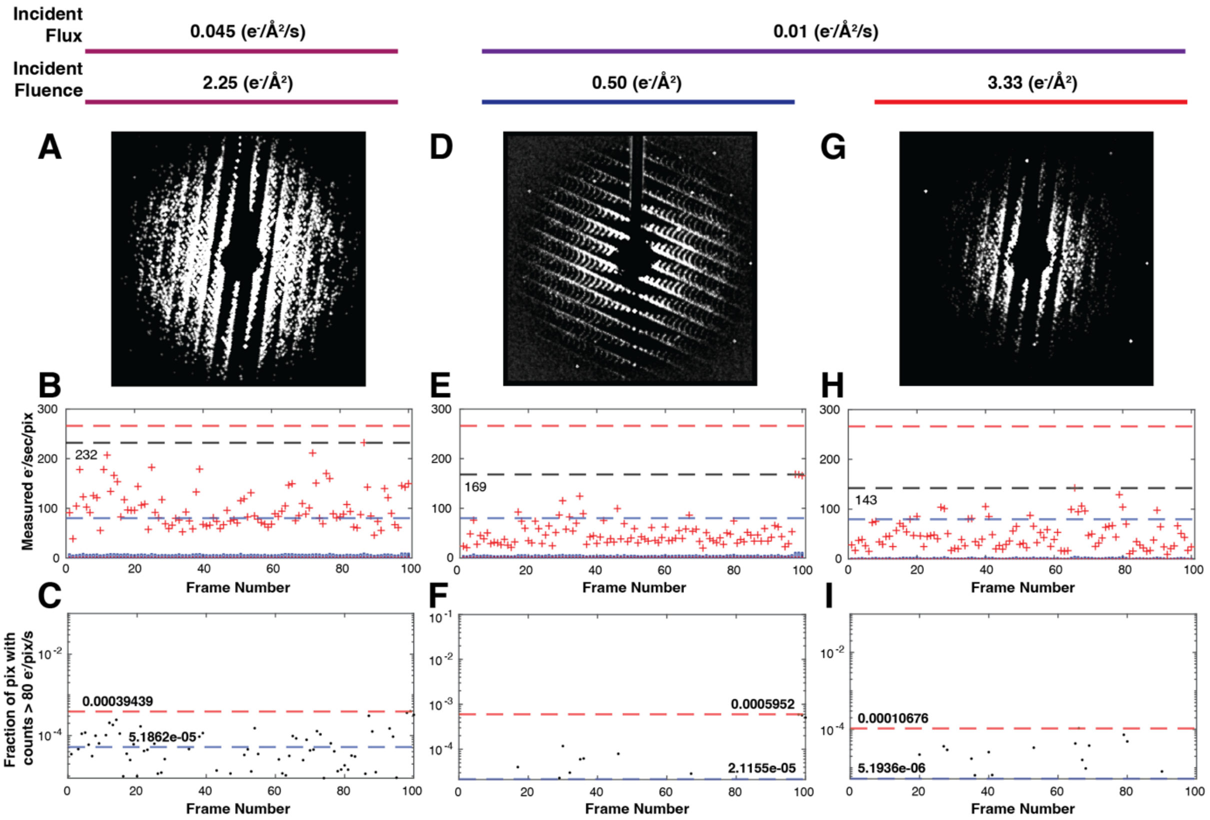

Supplementary figure 11. Analysis of electron counts across all frames of the three salen ligand datasets assessed in Supplementary Figure 5. Conditions differed in incident beam flux and total incident beam fluence, as indicated. Panels (A-C) here correspond to the highest incident beam flux, Sup Fig 5 Panel A; (D-E) here to Panel B; (G-I) to Sup Fig Panel C. In (B,E,H), blue bars span the mean value of counts per frame +/- one standard deviation. A dashed blue line in each left graph indicates a count of 80 e^-/pix/s, a dashed red line shows the maximum anticipated count rate of 266 e^-/pix/s, and a dashed black line the maximum counts observed across all frames. Red crosses indicate the maximum number of counts observed in each of the 100 patterns of a movie. Each point in (C,F,I) indicates the fraction of pixels in a frame whose counts exceed 80 e^-/pix/s; points are absent where no pixels exceed that threshold. In (C,F,I), dashed blue lines indicate the average fraction for that set of points, and dashed red lines indicate the maximum fraction observed in the set; their numerical values are indicated.

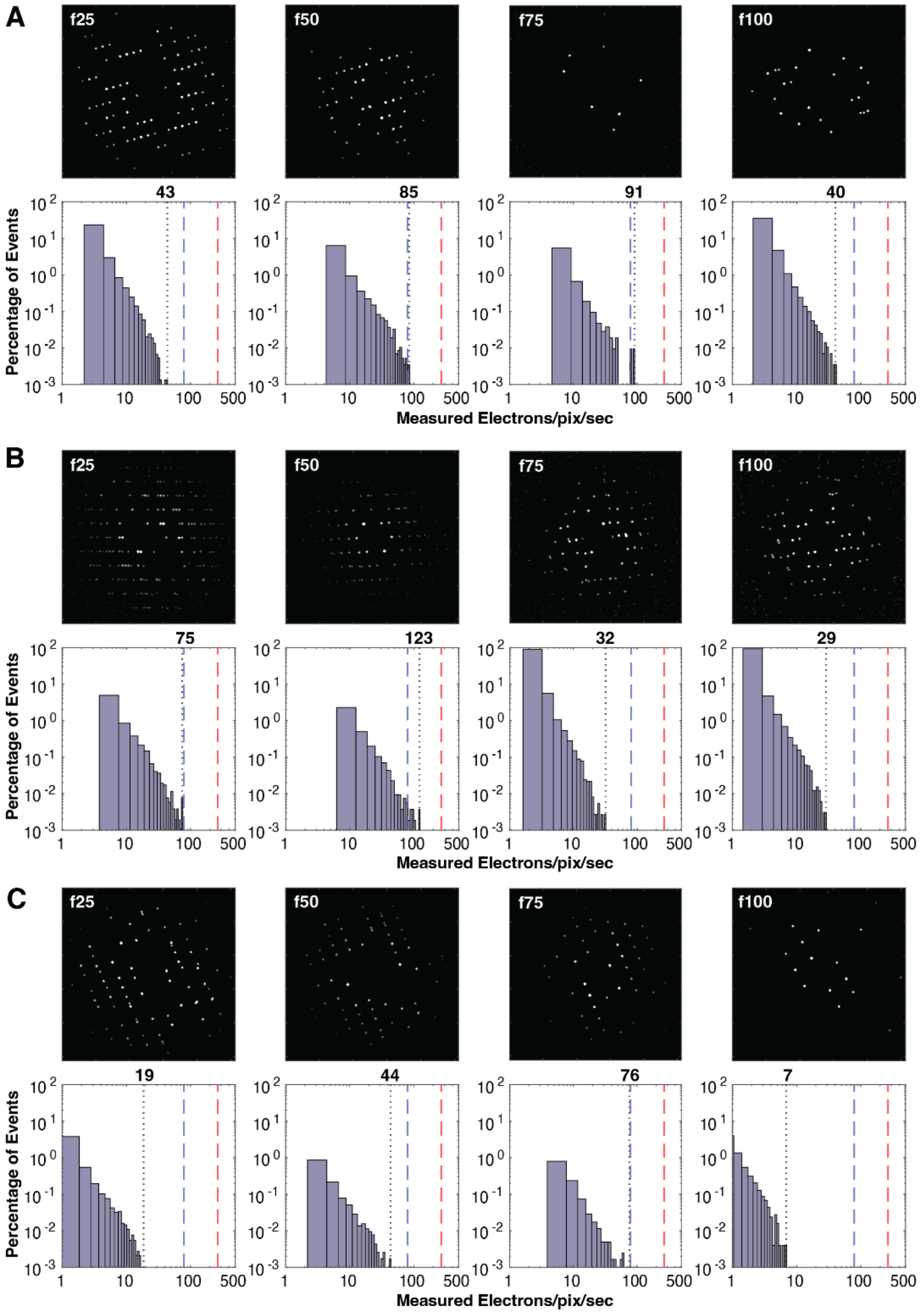

Supplementary figure 12. Representations of individual diffraction frames and histograms of electron count distributions for those frames, sampled from MicroED movies of biotin crystals. Reflections identified in each of four frames are shown; images correspond to frames 25, 50, 75 and 100 in a hundred-frame dataset. Three datasets sampled from three distinct biotin crystals are shown, with incident beam fluences of 2.25 (A) and 0.5 (B), and 3.33 (C) $e^-/Å^2$/s. On histogram plots, blue dashed lines denote 80 counted e^-/pix/s, red dashed lines indicate 266 e^-/pix/s, and black dashed lines indicate the maximum number of e^-/pix/s detected in the sampled frame. A dashed line and the number above it in histograms mark the maximum counts for each frame, in e^-/pix/s.

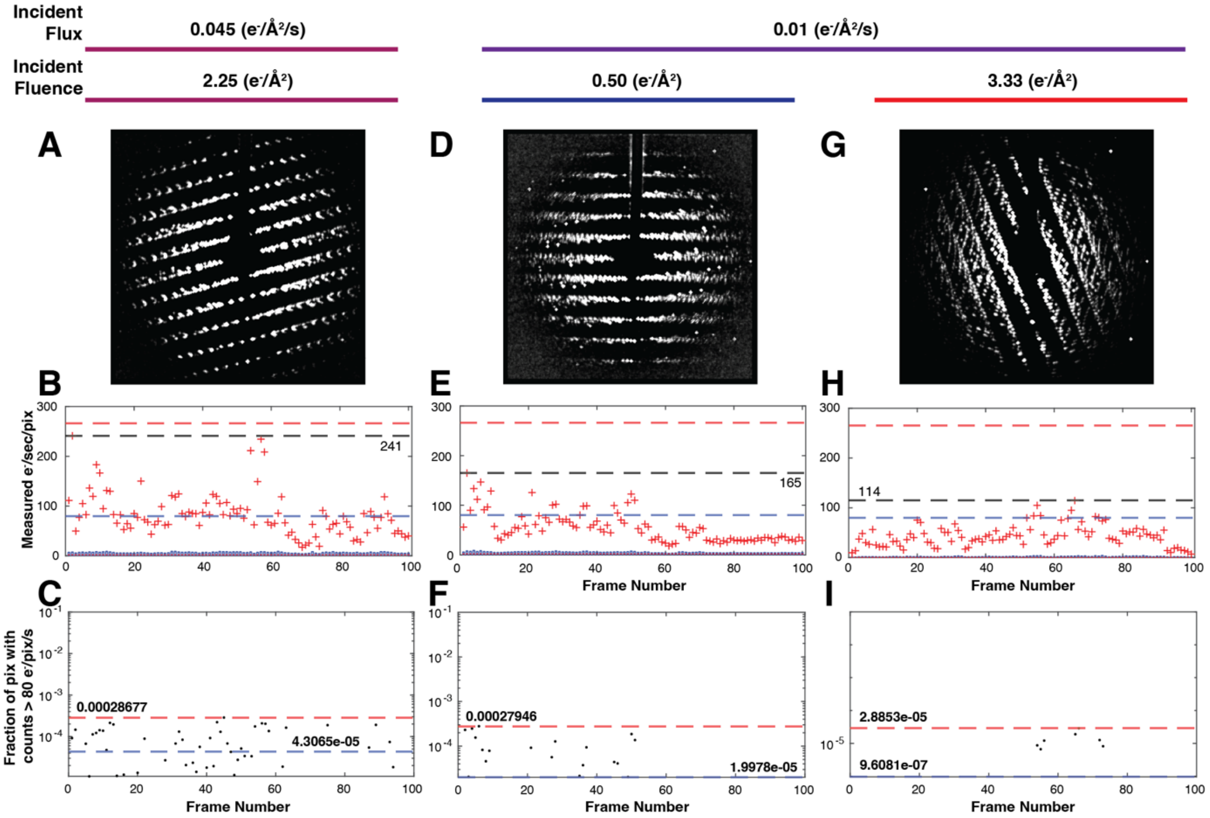

Supplementary figure 13. Analysis of electron counts across all frames of the biotin datasets assessed in Supplementary Figure 7. Conditions differed in incident beam flux and total incident beam fluence, as indicated. Panels (A-C) here correspond to the highest incident beam flux, Sup Fig 7 Panel A; (D-E) here to Panel B; (G-I) to Sup Fig Panel C. In (B,E,H), blue bars span the mean value of counts per frame +/- one standard deviation. A dashed blue line in each left graph indicates a count of 80 e$^-$/pix/s, a dashed red line shows the maximum anticipated count rate of 266 e$^-$/pix/s, and a dashed black line the maximum counts observed across all frames. Red crosses indicate the maximum number of counts observed in each of the 100 patterns of a movie. Each point in (C,F,I) indicates the fraction of pixels in a frame whose counts exceed 80 e$^-$/pix/s; points are absent where no pixels exceed that threshold. In (C,F,I), dashed blue lines indicate the average fraction for that set of points, and dashed red lines indicate the maximum fraction observed in the set; their numerical values are indicated.

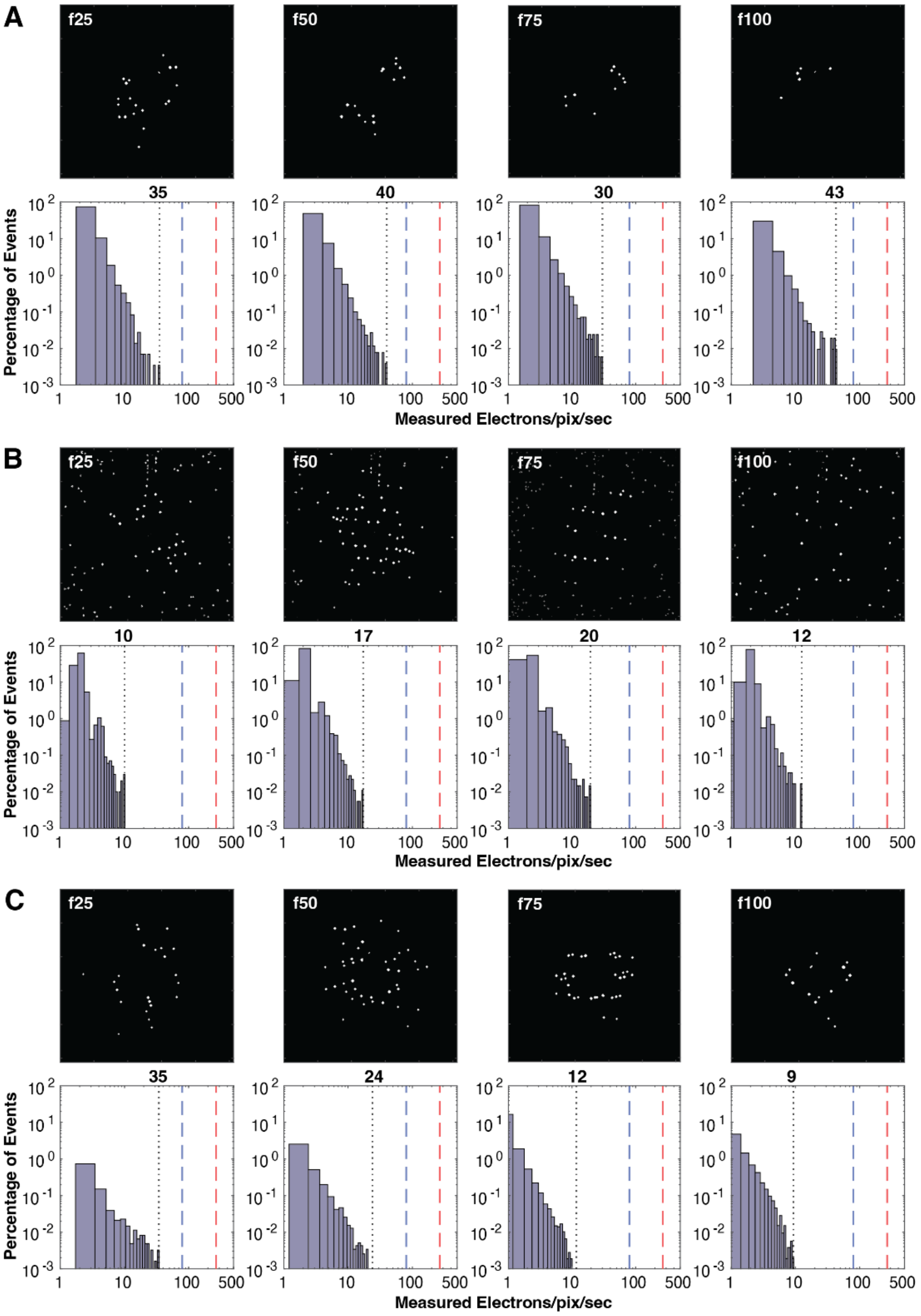

Supplementary figure 14. Representations of individual diffraction frames and histograms of electron count distributions for those frames, sampled from MicroED movies of thiostrepton crystals. Reflections identified in each of four frames are shown; images correspond to frames 25, 50, 75 and 100 in a hundred-frame dataset. Three datasets sampled from three distinct thiostrepton crystals are shown, with incident beam fluences of 2.25 (A) and 0.5 (B), and 3.33 (C) $e^-/Å^2/s$. On histogram plots, blue dashed lines denote 80 counted e^-/pix/s, red dashed lines indicate 266 e^-/pix/s, and black dashed lines indicate the maximum number of e^-/pix/s detected in the sampled frame. A dashed line and the number above it in histograms mark the maximum counts for each frame, in e^-/pix/s.

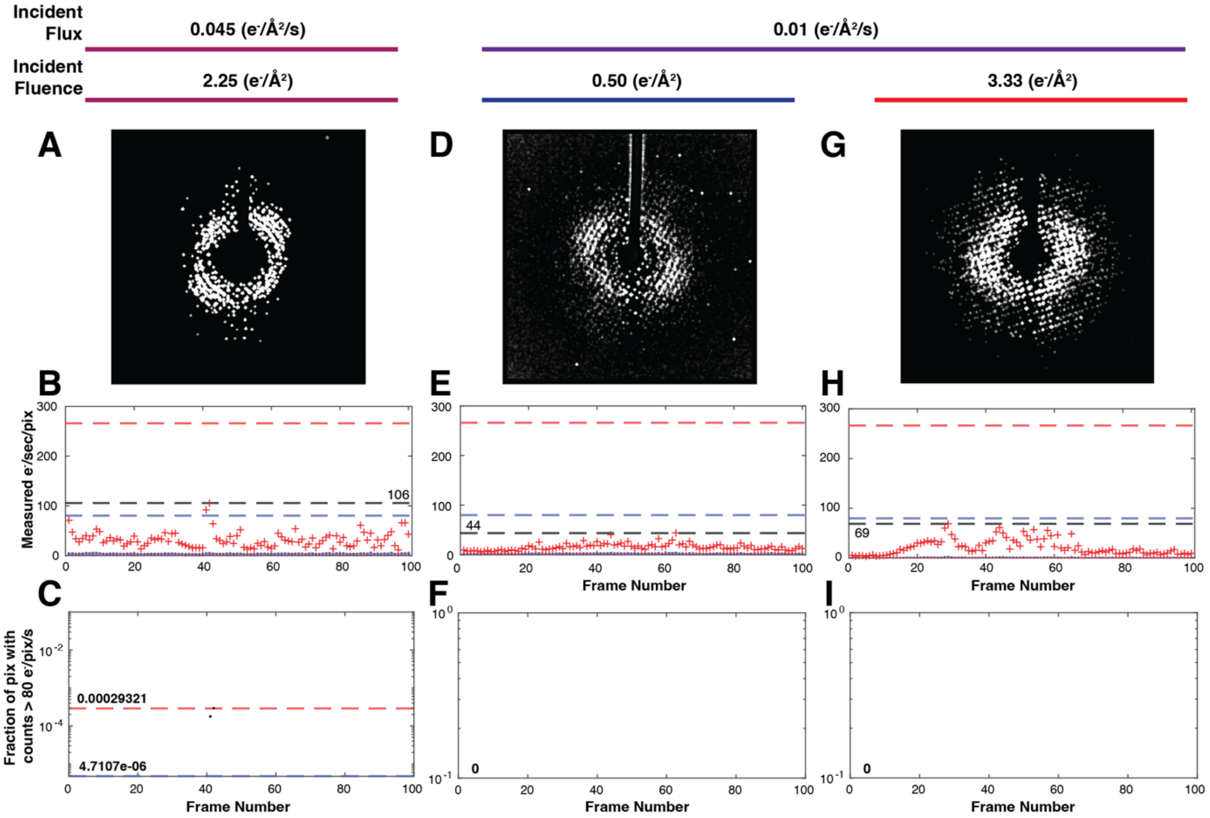

Supplementary figure 15. Analysis of electron counts across all frames of the thiostrepton datasets assessed in Supplementary Figure 9. Conditions differed in incident beam flux and total incident beam fluence, as indicated. Panels (A-C) here correspond to the highest incident beam flux, Sup Fig 9 Panel A; (D-E) here to Panel B; (G-I) to Sup Fig Panel C. In (B,E,H), blue bars span the mean value of counts per frame +/- one standard deviation. A dashed blue line in each left graph indicates a count of 80 e^-/pix/s, a dashed red line shows the maximum anticipated count rate of 266 e^-/pix/s, and a dashed black line the maximum counts observed across all frames. Red crosses indicate the maximum number of counts observed in each of the 100 patterns of a movie. Each point in (C,F,I) indicates the fraction of pixels in a frame whose counts exceed 80 e^-/pix/s; points are absent where no pixels exceed that threshold. In (C,F,I), dashed blue lines indicate the average fraction for that set of points, and dashed red lines indicate the maximum fraction observed in the set; their numerical values are indicated.

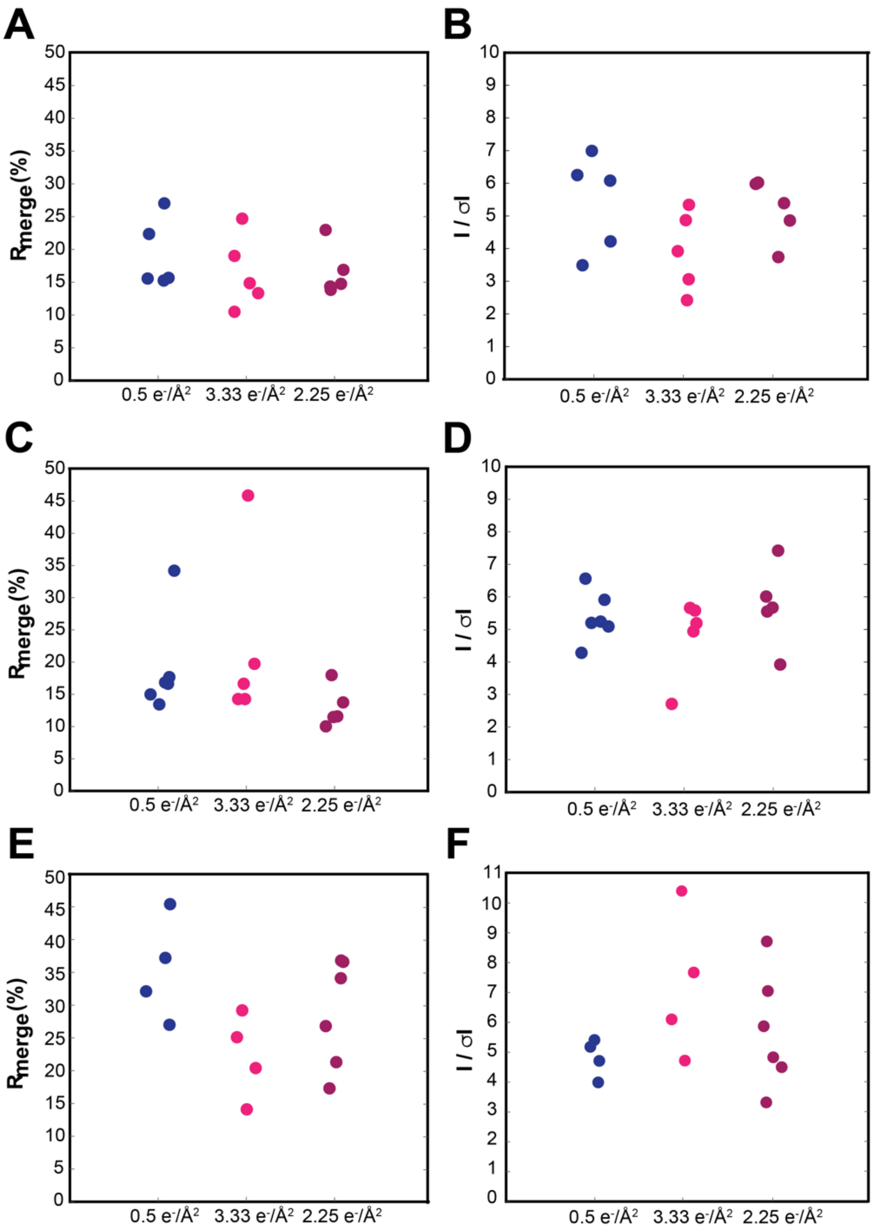

Supplementary figure 16. Analysis of EBEC MicroED data reduction statistics. Statistics for data collected with varying incident electron beam flux for salen ligand (A, B), biotin (C, D) and thiostrepton crystals (E, F). For each, the overall R_{merge} and I/sigma are shown for crystals sampled delivering a total fluence of 0.5 $e^-/Å^2$ (2 deg/s rotation, 2 integrated frames/s, 0.01 $e^-/Å^2$/s flux density, blue points), 3.33 0.5 $e^-/Å^2$ (0.3 deg/s rotation, 0.3 integrated frames/s, 0.01 $e^-/Å^2$/s flux density, pink points), and 2.25 $e^-/Å^2$ (2 deg/s rotation, 2 integrated frames/s, 0.045 $e^-/Å^2$/s flux density, magenta points). Reflections to a maximum resolution of 0.8 Å are considered for the salen ligand and biotin, and out to 2.0 Å for thiostrepton.

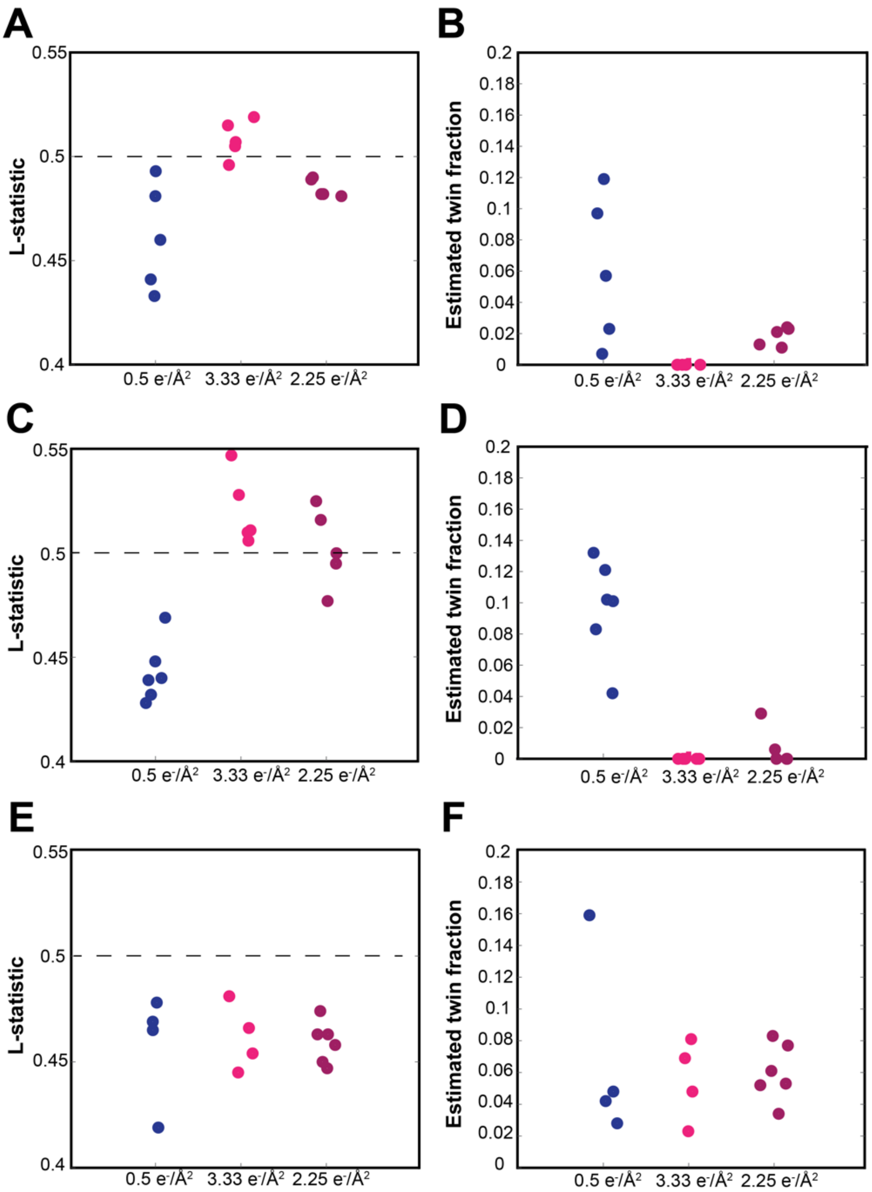

Supplementary figure 17. Analysis of L-test statistics vs. incident electron beam flux for datasets in Supplementary Figure 14. Plots show the L-statistic computed for each of the datasets of salen ligand (A), biotin (C) and thiostrepton (E) crystals, sampled delivering a total fluence of 0.5 e$^-$/Å^2 (2 deg/s rotation, 2 integrated frames/s, 0.01 e$^-$/Å^2/s flux density, blue points), 3.33 0.5 e$^-$/Å^2 (0.3 deg/s rotation, 0.3 integrated frames/s, 0.01 e$^-$/Å^2/s flux density, pink points), and 2.25 e$^-$/Å^2 (2 deg/s rotation, 2 integrated frames/s, 0.045 e$^-$/Å^2/s flux density, magenta points). A dashed black line indicates values above which data is considered perfectly un-twinned. Corresponding plots of the estimated twin fraction for each crystal are computed from the L statistic for salen ligand (B), biotin (D) and thiostrepton (F) crystals.

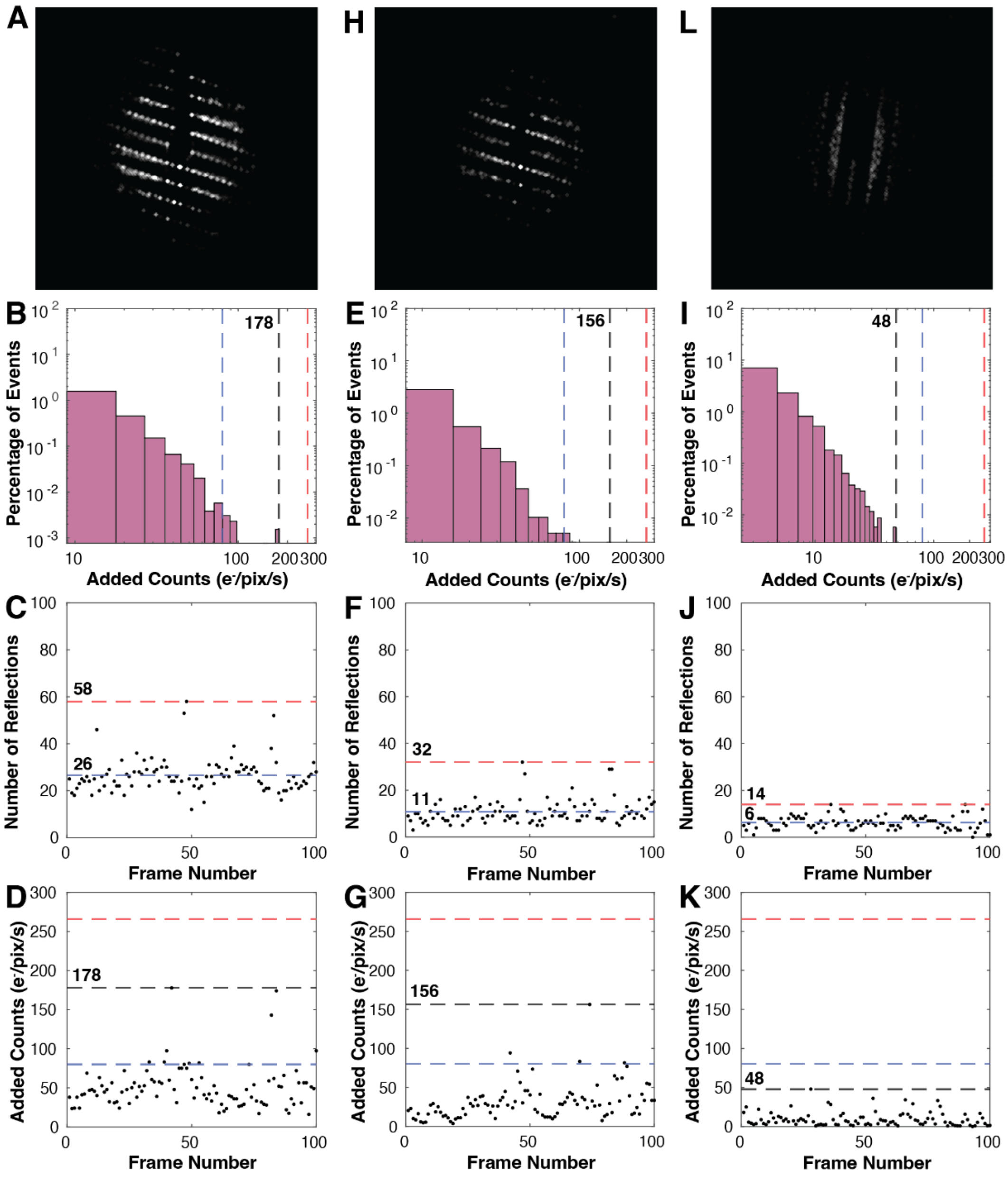

Supplementary figure 18. The impact of CL-adjustment on EBEC MicroED data collected from salen ligand crystals. Analyses of three representative crystal datasets are shown, across various incident beam flux and fluence settings: a flux of 0.045 $e^-/Å^2/s$ (A-D), 0.01 $e^-/Å^2/s$ (H-K); a fluence of 2.25 $e^-/Å^2$ (A-D), 0.5 $e^-/Å^2$ (H-G), 3.33 $e^-/Å^2$ (L-K). For each, a pattern shows the locations of all reflections that received a CL-adjustment (A,H,L), a histogram of all added counts across the entire movie (B,E,I), the total number of reflections adjusted per frame, across all frames in a dataset (C,F,J), and the maximum number of electron counts added for any given pixel in a frame, for all frames in a dataset (D,G,K). In (B,D,E,G,I,K), dashed red lines indicate 266 e^-/pix/s, dashed blue lines indicate 80 e^-/pix/s; dashed black lines indicate maximum electron counts added for the whole dataset. In (C,F,J), dashed red lines indicate maximum number of reflections adjusted in a given frame of the dataset; dashed blue lines indicate the mean number of reflections adjusted per frame over the dataset. Resolution rings are labeled in (A,H,L).

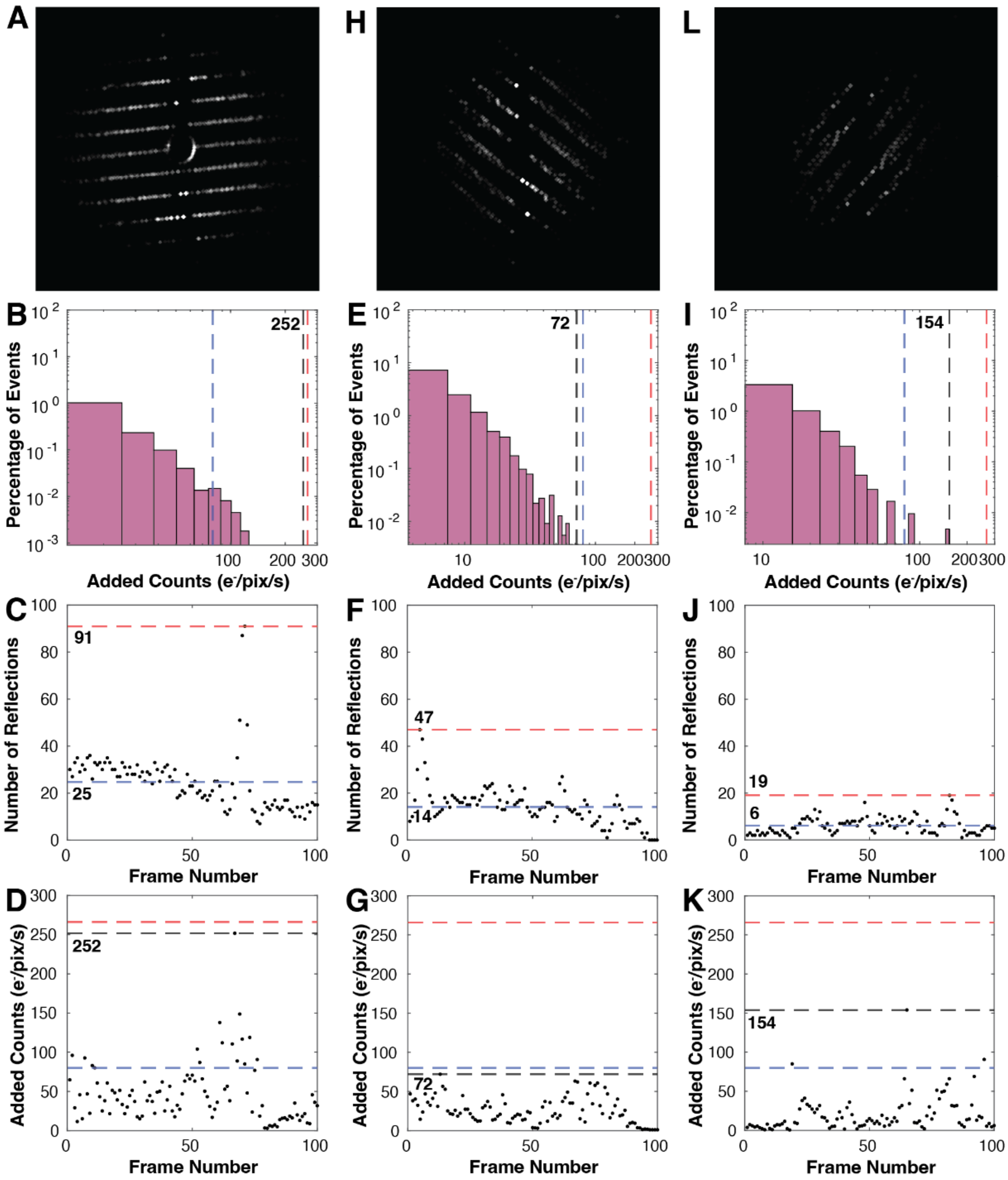

Supplementary figure 19. The impact of CL-adjustment on EBEC MicroED data collected from biotin crystals. Analyses of three representative crystal datasets are shown, across various incident beam flux and fluence settings: a flux of 0.045 e$^-$/Å^2/s (A-D), 0.01 e$^-$/Å^2/s (H-K); a fluence of 2.25 e$^-$/Å^2 (A-D), 0.5 e$^-$/Å^2 (H-G), 3.33 e$^-$/Å^2 (L-K). For each, a pattern shows the locations of all reflections that received a CL-adjustment (A,H,L), a histogram of all added counts across the entire movie (B,E,I), the total number of reflections adjusted per frame, across all frames in a dataset (C,F,J), and the maximum number of electron counts added for any given pixel in a frame, for all frames in a dataset (D,G,K). In (B,D,E,G,I,K), dashed red lines indicate 266 e$^-$/pix/s, dashed blue lines indicate 80 e$^-$/pix/s; dashed black lines indicate maximum electron counts added for the whole dataset. In (C,F,J), dashed red lines indicate maximum number of reflections adjusted in a given frame of the dataset; dashed blue lines indicate the mean number of reflections adjusted per frame over the dataset. Resolution rings are labeled in (A,H,L).

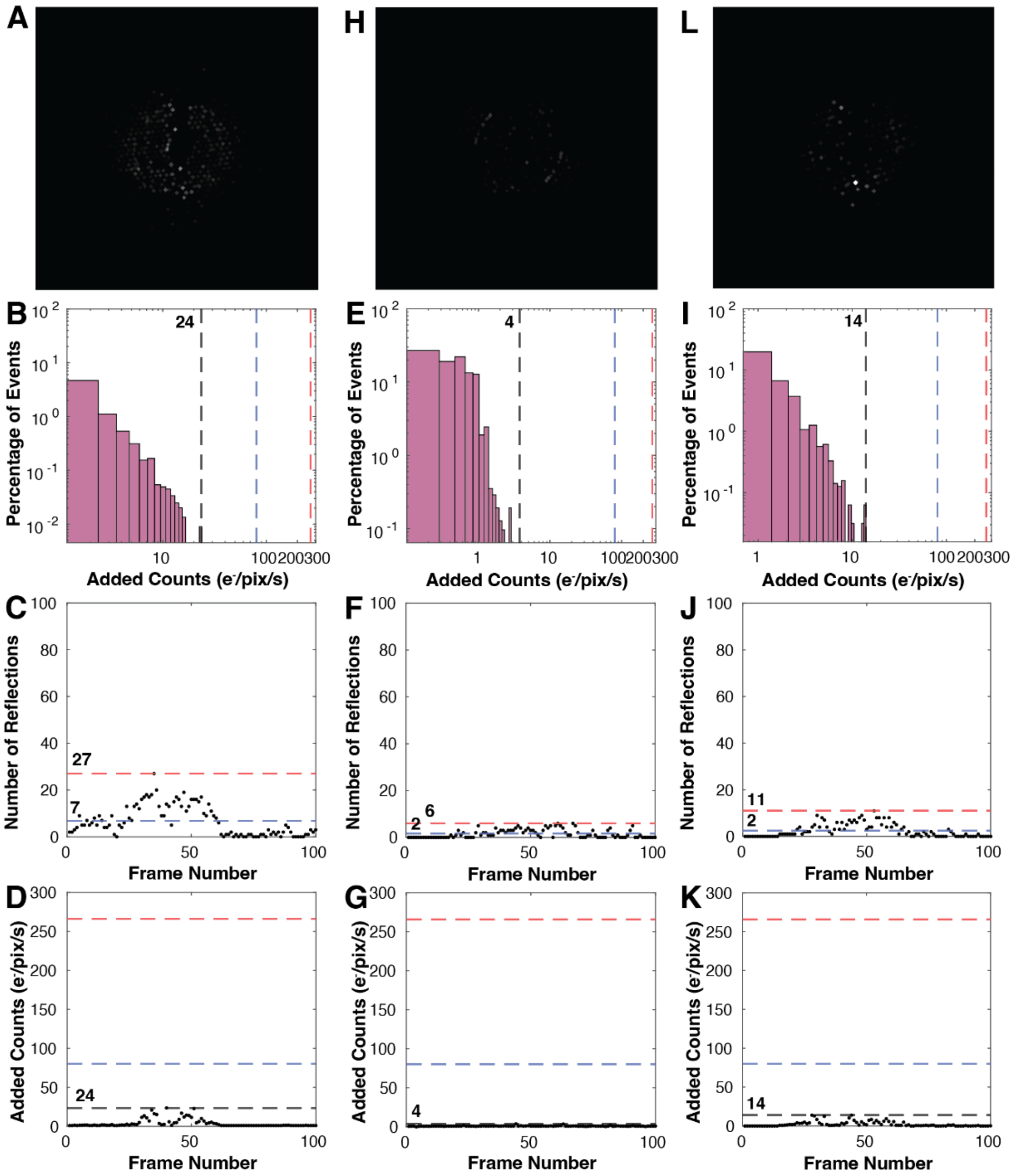

Supplementary figure 20. The impact of CL-adjustment on EBEC MicroED data collected from thiostrepton crystals. Analyses of three representative crystal datasets are shown, across various incident beam flux and fluence settings: a flux of 0.045 $e^-/Å^2/s$ (A-D), 0.01 $e^-/Å^2/s$ (H-K); a fluence of 2.25 $e^-/Å^2$ (A-D), 0.5 $e^-/Å^2$ (H-G), 3.33 $e^-/Å^2$ (L-K). For each, a pattern shows the locations of all reflections that received a CL-adjustment (A,H,L), a histogram of all added counts across the entire movie (B,E,I), the total number of reflections adjusted per frame, across all frames in a dataset (C,F,J), and the maximum number of electron counts added for any given pixel in a frame, for all frames in a dataset (D,G,K). In (B,D,E,G,I,K), dashed red lines indicate 266 e^-/pix/s, dashed blue lines indicate 80 e^-/pix/s; dashed black lines indicate maximum electron counts added for the whole dataset. In (C,F,J), dashed red lines indicate maximum number of reflections adjusted in a given frame of the dataset; dashed blue lines indicate the mean number of reflections adjusted per frame over the dataset. Resolution rings are labeled in (A,H,L).